

Water Resources Research®

RESEARCH ARTICLE

10.1029/2022WR033097

Key Points:

- This study demonstrated the potential to support multi-dimensional flow model development on a large river using remotely sensed bathymetry
- Hyperspectral imagery acquired via piloted/uncrewed aircraft was more suitable than multispectral imagery for parameterizing flow models
- Modeled salmon habitat metrics were less sensitive than bioenergetic predictions of fish movement to source bathymetry

Correspondence to:





L. R. Harrison,
lee.harrison@noaa.gov

Citation:

Harrison, L. R., Legleiter, C. J., Sridharan, V. K., Dudley, P. N., & Daniels, M. E. (2022). Evaluating the sensitivity of multi-dimensional model predictions of salmon habitat to the source of remotely sensed river bathymetry. *Water Resources Research*, 58, e2022WR033097. <https://doi.org/10.1029/2022WR033097>

Received 21 JUN 2022
Accepted 8 DEC 2022

Evaluating the Sensitivity of Multi-Dimensional Model Predictions of Salmon Habitat to the Source of Remotely Sensed River Bathymetry

Lee R. Harrison^{1,2} , Carl J. Legleiter³ , Vamsi K. Sridharan^{1,4} , Peter N. Dudley^{1,4}, and Miles E. Daniels^{1,4} 

¹National Oceanic and Atmospheric Administration, Southwest Fisheries Science Center, Santa Cruz, CA, USA, ²Earth Research Institute, University of California, Santa Barbara, CA, USA, ³U.S. Geological Survey, Observing Systems Division, Golden, CO, USA, ⁴Institute of Marine Sciences, University of California, Santa Cruz, CA, USA

Abstract Multi-dimensional numerical models are fundamental tools for investigating biophysical processes in aquatic ecosystems. Remote sensing techniques increase the feasibility of applying such models at riverscape scales, but tests of model performance on large rivers have been limited. We evaluated the potential to develop two-dimensional (2D) and three-dimensional (3D) hydrodynamic models for a 1.6-km reach of a large gravel-bed river using three sources of remotely sensed river bathymetry. We estimated depth from hyperspectral image data acquired from conventional and uncrewed aircraft and multispectral satellite imagery. Our results indicated that modeled water depth errors were similar between 2D and 3D models, with depth residuals that were comparable to the uncertainty associated with the bathymetry used as input. We found good agreement between measured and modeled depth-averaged velocities generated by 2D and 3D models, while 3D models provided superior predictions of near-bed velocities. We found that optimal model performance occurred for lower flow resistance values than previously reported in the literature, possibly as a consequence of the high-resolution bathymetry used as model input. Model predictions of winter-run Chinook salmon (*Oncorhynchus tshawytscha*) spawning and rearing habitat were not sensitive to the source of bathymetric information, but bioenergetic predictions related to adult holding costs were influenced by the input bathymetry. Our results suggest that hyperspectral imagery acquired from piloted and/or uncrewed aircraft can be used to map the bathymetry of clear-flowing, relatively shallow large rivers with sufficient accuracy to support multi-dimensional flow model development; models developed from multispectral satellite imagery had more limited predictive capability.

1. Introduction

Numerical models have become essential tools for investigating biophysical processes in river ecosystems (Reeder et al., 2021) and informing decisions related to water resources management (Benjankar et al., 2018), and ecological conservation (Wheaton et al., 2018). Multi-dimensional numerical models provide a means of exploring interactions between flow fields, sediment transport, and river morphology in two or three dimensions (2D or 3D) (Shimizu et al., 2020). Models are widely used in aquatic habitat studies (Brown & Pasternack, 2009; Kammel et al., 2016; May et al., 2009; May & Pryor, 2016) and in process-based, bioenergetic analyses of flow-species interactions (Jowett et al., 2021). Multi-dimensional models are key tools in river restoration design (Brown, 2022) and also provide a means of quantifying morphodynamic processes in channels and riparian zones following restoration (Vargas-Luna et al., 2018).

The performance of 2D and 3D models is dependent on boundary conditions, and accurate bathymetric data are an essential requirement for numerical modeling (Pasternack, 2019). Recent advances in fluvial remote sensing have enabled acquisition of continuous, high resolution bathymetric data (Carbonneau et al., 2012; Piégay et al., 2020), thereby facilitating development of ecohydraulic models at longer, river segment scales (Benjankar et al., 2019). Remote sensing provides an appealing alternative to traditional field-based surveying techniques, which are time consuming and generally limited to short, isolated reaches. However, while remote sensing can provide extensive, highly detailed bathymetric data, the errors inherent to these data might be larger than those associated with conventional field surveys. Thus, an important unresolved question is how errors in different types of remotely sensed bathymetry data influence the accuracy of ecohydraulic model predictions.

Several approaches to acquiring continuous, high resolution topographic and bathymetric (topo-bathymetric) data are in common use. Airborne light detection and ranging (lidar) data, collected using near-infrared (NIR) wavelength ($\lambda = 1,064$ nm) lasers, are routinely used to measure terrestrial topography, such as river bars, banks, and floodplains (Mandlbürger et al., 2015). NIR lidar data have become the standard for mapping topographic surfaces, with vertical accuracy on the order of a few cm (Passalacqua et al., 2015). Bathymetric lidar sensors, which use green wavelength ($\lambda = 532$ nm) lasers, have been successfully used to map submerged bathymetry on small to medium rivers with decimeter-scale accuracy (McKean et al., 2009; Tonina et al., 2018). On larger rivers, green lidar might be capable of measuring river bathymetry only up to a maximum detectable depth of ~ 3 m (Lague & Feldmann, 2020). Lidar data have traditionally been obtained from airborne platforms but smaller, uncrewed aerial system (UAS) lidar sensors have emerged more recently (Kinzel et al., 2021; Mandlbürger et al., 2020).

Spectrally based remote sensing provides another option for mapping water depths based on differences in the rate at which solar radiation of different wavelengths is attenuated by the water column. Spectrally based approaches have been used to map water depth using true color, multispectral, and hyperspectral imagery (Legleiter et al., 2009; Lyzenga, 1978; Winterbottom & Gilvear, 1997). This type of depth retrieval is best-suited to shallow, clear-flowing rivers with water depths up to approximately 2–3 m, but greater maximum detectable depths have been reported on certain larger rivers (Legleiter & Fosness, 2019). Conversely, spectrally based techniques cannot be applied to more turbid rivers due to limited penetration of light through the water column. Under appropriate conditions, passive optical approaches provide a means of estimating water depths that can be converted to bathymetry by subtracting the depth estimates from water surface elevations obtained from lidar sensors to produce hybrid, topo-bathymetric digital elevation models (DEMs) (Legleiter, 2021). Image-based bathymetric mapping has been conducted using airborne platforms (O’Sullivan et al., 2021) and satellites (Niroumand-Jadidi et al., 2018). Structure-from-Motion (SfM) photogrammetric techniques have also been used to infer water depth from images via small UAS (Dietrich, 2017; Woodget et al., 2015).

Both green lidar- and image-based bathymetry have been used as input for developing multi-dimensional flow models. Previous studies have demonstrated the ability to develop 2D models based on bathymetric lidar DEMs from a number of gravel-bed rivers, with errors comparable to models based on conventional field surveys (Mandlbürger et al., 2015; McKean et al., 2014; Tonina et al., 2020). Similarly, spectrally based bathymetric DEMs have been used as input for 2D flow models for evaluating hydraulic habitat (Tammenga et al., 2015), examining braided river flow dynamics (Javernick et al., 2016), and to simulate channel morphodynamics (Williams et al., 2016). While previous studies have demonstrated the potential of remotely sensed data to support 2D model development, the majority of these studies have been conducted on small to medium-sized rivers and relatively little is known regarding the applicability of these approaches to larger rivers (100 m or wider). Furthermore, the potential for developing 3D models using remotely sensed bathymetry has not yet been tested.

From an ecological perspective, many populations of California’s Pacific salmon (*Oncorhynchus* spp.) are critically endangered (Moyle et al., 2017). Their habitats are subject to numerous existential threats, including restricted access to historic habitats by water supply infrastructure, rising water temperatures, uncertain flows, and increasing human demand for water, all exacerbated by climate change (Crozier et al., 2019). In this context, accurate 2D and 3D numerical model evaluation of remaining riverine habitats is crucially important. Confidence in these assessments is contingent upon a quantitative understanding of how errors in the input bathymetric data propagate through a model and lead to errors in predictions of depth, velocity, and derived habitat variables.

Our research was organized around the following objectives:

1. Evaluate the potential to develop 2D and 3D hydrodynamic models for a large gravel-bed river using river bathymetries derived from airborne hyperspectral, UAS-based hyperspectral, and multispectral satellite imagery as model input.
2. Quantify model performance and compare errors in predicted salmon habitat quality metrics for each source of bathymetric information.

2. Materials and Methods

2.1. Study Area

The Sacramento River is located in California's Central Valley and is the state's largest river, with a drainage area of 6.8×10^4 km². Flow in the upper Sacramento is regulated by Shasta and Keswick Dams and the mean annual discharge measured at the USGS streamgage (site no. 11377100) near Red Bluff, CA, is 357 m³/s (U.S. Geological Survey, 2022). These two dams are migration barriers for salmon and prevent access to historical habitat in upstream tributaries. Downstream of Keswick Dam the mainstem river is used by three populations of Chinook salmon listed under the Endangered Species Act (Moyle et al., 2017).

Winter-run Chinook salmon (*Oncorhynchus tshawytscha*) use the Sacramento River downstream from Keswick Dam to complete the freshwater portion of their life cycle (Moyle et al., 2017). The anadromous, winter-run life cycle consists of upstream migration of adults returning from the Pacific Ocean in January through May each year. Adult winter-run hold in deep pools with good cover for several months and typically spawn in pools between April and August. Winter-run fry emerge from gravel substrates in July through October and juveniles rear for approximately five to 10 months before migrating downstream toward the Pacific Ocean (Yoshiyama et al., 1998). The 50% exceedance flows between 1964 and 2021 at the USGS streamgage (site no. 11377100) near Red Bluff during spawning, rearing, and holding life stages were 326, 250, and 276 m³/s, respectively (U.S. Geological Survey, 2022).

We focused on a 1.6 km reach of the Sacramento River near the confluence with Cottonwood Creek (Figure 1) that was the subject of a prior investigation on remote sensing of river bathymetry (Legleiter & Harrison, 2019a). Relative to areas farther upstream closer to Keswick Dam where water temperatures are generally cooler, winter-run Chinook salmon redd densities are lower in this location. The study area features a large meander bend, with Cottonwood Creek entering from the right bank (i.e., from the west) near the bend apex (near cross section (XS) #6; Figure 1). This reach has a gravel bed with a median sediment grain size (D_{50}) of 0.056 m, a D_{90} of 0.097 m (Singer, 2008), and a slope of 0.00097 m/m. At the time of our field campaign in September 2017, the mean wetted width was 111 m and the mean depth was 1.77 m (Figure 2). The reach is characterized by deep, pool habitat along the upstream (XS # 1–3) and downstream portions of the reach (XS# 8–9). A channel width constriction near XS# 4 increases the flow velocity, resulting in fast, deep run habitat along the curved portion of the reach (XS# 4–7). Slow-shallow habitat exists along the channel margins, at the confluence with Cottonwood Creek, and in a small alcove located beyond the bend apex (XS# 8).

2.2. Field Data

Field data collection and image acquisition occurred under low flow conditions, with a measured discharge of 260 m³/s (U.S. Geological Survey, 2022). The discharge measured on Cottonwood Creek at USGS site no. 11376000 was 1.6 m³/s (U.S. Geological Survey, 2022), a negligible amount compared to the flow in the mainstem Sacramento River. The turbidity measured at the time the field-based and remotely sensed data were collected was 3.3 NTU (Legleiter & Harrison, 2019a). We measured water depths by wading shallow areas of the channel and using a jet boat in deeper portions of the river. For the wading surveys, we used Real-Time Kinematic Global Navigation Satellite System (RTK-GNSS) equipment to record water-surface elevations (WSE) along the edge of the wetted channel and bed elevations in shallow areas safely accessible from the bank. We calculated wading depths by subtracting each bed elevation measurement from the nearest WSE observation.

For the deeper portions of the channel, we measured water depth using a single-beam echosounder and also collected data on water depth and velocity with a SonTek S5 acoustic Doppler current profiler (ADCP). We deployed the echo sounder and ADCP from a jet boat and surveyed 10 cross sections (XS) (Figure 1), making 4–10 passes across the channel at each XS. The ADCP was equipped with an integrated differential GPS with a horizontal accuracy of 0.15–0.2 m. We used the Velocity Mapping Toolbox (VMT) (Parsons et al., 2013) to: (a) project ADCP transects onto a grid with a horizontal and vertical spacing of 1 and 0.1 m, respectively; (b) rotate velocity data onto a common plane; and (c) smooth velocity ensembles using a nearest neighbor approach. In areas where the ADCP did not measure near-bed velocities reliably (the lowermost 10% of the flow depth), we fitted a logarithmic profile to the measured part of the flow field and projected from the lowermost valid velocity measurement to zero velocity at the bed.

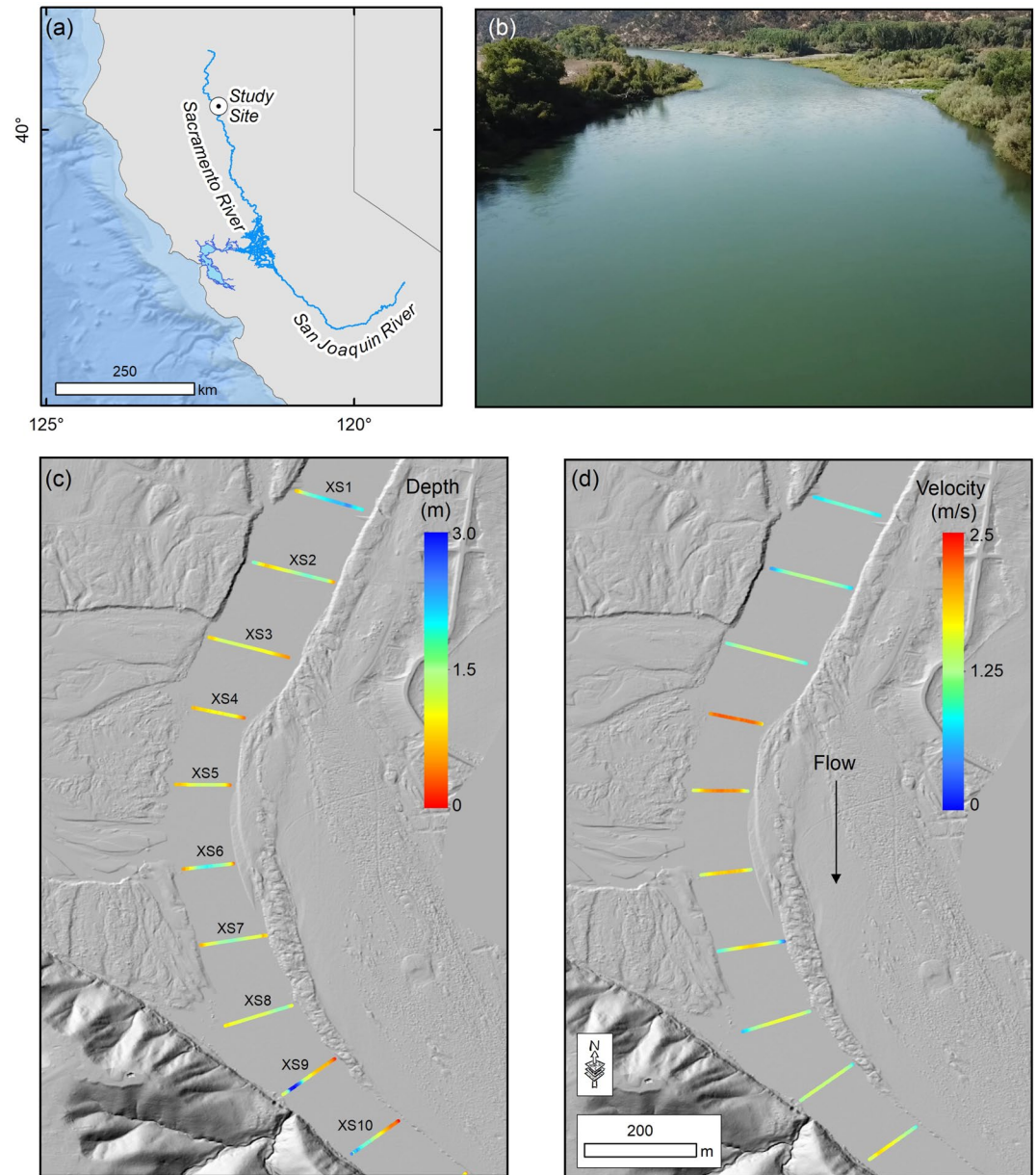


Figure 1. (a) Location of the Sacramento River in northern California, USA. (b) Oblique aerial image of the study reach, where the view is looking downstream from the top of the reach. (c) Field-based acoustic Doppler current profiler (ADCP) depth and (d) depth-averaged velocity measurements overlain on a hillshade image produced from lidar topography. Data sources in panel (a) include Esri, Garmin, GEBCO, NOAA, and USGS.

2.3. Remote Sensing Data

We leveraged remotely sensed river bathymetry data from a previous study on the same reach (Legleiter & Harrison, 2019a) that evaluated the potential to map water depths using a generalized version of the Optimal Band Ratio Analysis (OBRA) framework introduced by Legleiter et al. (2009). This method uses ratios of spectral bands to calculate an image-derived quantity X , defined as:

$$X = \ln \left[\frac{R(\lambda_1)}{R(\lambda_2)} \right], \quad (1)$$

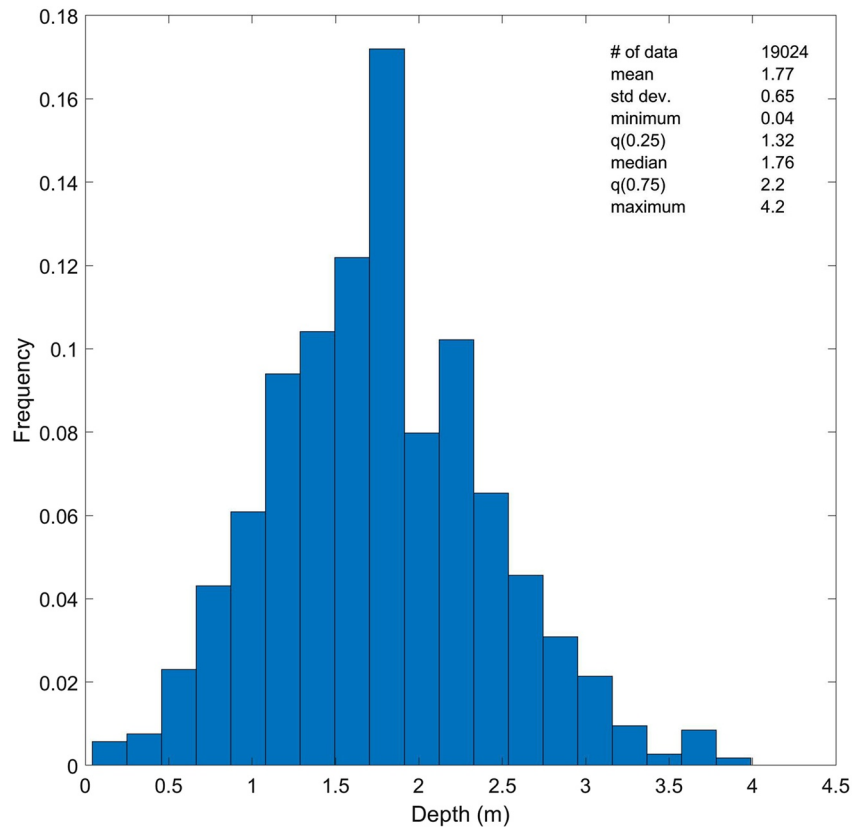


Figure 2. Histogram and summary statistics for measured water depth data.

where $R(\lambda_1)$ and $R(\lambda_2)$ are reflectances recorded in numerator and denominator bands centered at wavelengths λ_1 and λ_2 , respectively. The OBRA algorithm uses paired observations of depth and $R(\lambda)$ to calculate X values for all possible band combinations and then regresses X against depth for each version of X . The optimal band ratio is taken to be that λ_1 and λ_2 pair that produces the highest coefficient of determination R^2 .

Legleiter and Harrison (2019a) used OBRA to map water depths from hyperspectral data collected from piloted and uncrewed aircraft and a multispectral satellite image. The airborne hyperspectral data were acquired with a Compact Airborne Spectrographic Imager (CASI) 1500H (ITRES, 2014) deployed on a Cessna Caravan. The UAS-based hyperspectral image was acquired from a DJI Matrice 600 UAS equipped with a compact Nano-Hyperspec (Nano) imaging system (Headwall Photonics, 2018). The multispectral image was acquired by the WorldView-3 (WV3) satellite. The airborne hyperspectral (CASI), UAS hyperspectral (Nano), and satellite multispectral (WV3) data had native image pixel sizes of 0.5, 0.18, and 1.36 m, respectively. Previous OBRA results from this reach indicated that the airborne hyperspectral imagery provided the most accurate depths, followed by the UAS hyperspectral, and then satellite multispectral (Legleiter & Harrison, 2019a), with depth errors of 14%, 16%, and 19% of the mean depth, respectively (Table 1). Legleiter and Harrison (2019a) compared

Table 1
Summary of Remote Sensing Data and Depth Retrieval Errors

Sensor	Data type	Height (km)	Pixel size (m)	Bands	Wavelengths (nm)	Depth RMSE (%)
CASI 1500H	Airborne hyperspectral	1	0.5	48	373–1,043	14
Nano-Hyperspec	UAS-based hyperspectral	0.12	0.18	276	396–1,005	16
WorldView-3	Satellite multispectral	617	1.36	8	400–954	19

Note. Optimal Band Ratio Analysis (OBRA) depth RMSE values based on Legleiter and Harrison (2019a).

several different formulations of the X versus depth relation and in this study we followed their recommendation to produce depth maps using an exponential function.

In this study, we generated hybrid, topo-bathymetric DEMs for each imagery data set via the following workflow. We used an airborne NIR lidar DEM of the entire reach to obtain elevations on dry land and the water surface. We then subtracted image-based depth estimates from the water surface to convert depths to bed elevations and fused these points with the lidar data to make a continuous DEM. This process was repeated for the airborne hyperspectral, UAS hyperspectral and satellite multispectral datasets, resulting in three different DEMs, each with a resolution of 1 m. The field and remotely sensed data used in this study are available from USGS data releases (Legleiter & Harrison, 2019b; Legleiter & Harrison, 2022).

2.4. Hydrodynamic Modeling

We used the Delft3D-Flexible Mesh (Delft3D-FM) model developed by Deltares (2022) to predict 2D and 3D flow hydraulics in the study reach for each of the three source bathymetries. Delft3D is one of the most widely used models to simulate 2D and 3D hydrodynamics (Kasvi et al., 2015; Schuurman et al., 2018; Wegscheider et al., 2021; Wheaton et al., 2018; Williams et al., 2016). Delft3D-FM solves the Reynolds averaged Navier–Stokes (RANS) equations using a finite-volume method. We used a curvilinear grid with a cell size of 1 m. For the 2D models, we included a spiral flow parameter, which accounts for the effects of secondary flow induced by streamline curvature. For the 3D models, the vertical grid was divided into 10 σ -layers that followed the bottom topography and free surface. Each σ -layer represented 10% of the flow depth. We set the time step to ensure a Courant number less than 0.7 (Deltares, 2022), and specified a minimum depth for wetting/drying calculations of 0.05 m.

The models require specification of the upstream discharge, downstream stage, flow resistance, and turbulence closure scheme. We prescribed an upstream discharge of 260 m³/s and ran steady flow simulations. The flow resistance was defined using a uniform roughness height, k_s , which was converted to spatially explicit Chezy C coefficients via the Colebrook-White equation:

$$C = 18 \log \frac{12H}{k_s}, \quad (2)$$

where H is the water depth (m) and k_s is the Nikuradse roughness height (m). The roughness height, k_s , is commonly calculated as the product of a multiplicative factor, α_s , and a representative bed sediment grain size diameter, D_x :

$$k_s = \alpha_s D_x, \quad (3)$$

Here, we defined D_x to be D_{90} (0.097 m), which represents sediment grains that protrude into the flow. A wide range of roughness height values have been reported in the literature (García, 2008). We performed a sensitivity analysis on the 2D models by varying the bed roughness between approximately $0.5D_{90}$ and $1.5D_{90}$. Results from this analysis indicated that a k_s value of 0.12 m ($\alpha_s \approx 1.2$) provided the best agreement between measured and modeled depths and we adopted this value for both 2D and 3D models. We used the same reach-averaged k_s value for all models in order to quantify the error associated with each bathymetry, based on grain size data collected 400 m from our study reach by Singer (2008). We acknowledge that using a single reach-averaged k_s value does not capture local-scale sediment patches, which can influence flow hydraulics (Tonina et al., 2020). However, collecting such patch-scale bed surface grain size data in the Sacramento River during our field campaign was not feasible.

To account for turbulence in the 2D model, we used a uniform eddy viscosity. We evaluated the model's sensitivity to this parameter by varying the eddy viscosity between 0.1 and 1 m²/s and found that a value of 1 m²/s provided the closest agreement with measured velocities. While this value is high it is within the range of values reported in the literature for Delft3D-FM models (Barrera Crespo et al., 2019; Martyr-Koller et al., 2017; Willemssen et al., 2022). The specified eddy viscosity value maintained model stability and successfully reproduced the flow fields. For the 3D model, turbulence was represented using a κ - ϵ turbulence closure model (Deltares, 2022).

2.5. Accuracy Assessment

We used the calibrated 2D and 3D models to predict water depth and velocity for each bathymetry source and compared measured and modeled values. We used a channel-centered, orthogonal curvilinear (s, n) coordinate system for both the model output and ADCP transect data in order to facilitate comparison between observed and predicted hydraulic quantities in the streamwise and cross-stream directions. Hydrodynamic model performance was evaluated based on depth and velocity errors, $\epsilon(\mathbf{s})$, calculated as:

$$\epsilon(\mathbf{s}) = P_f(\mathbf{s}) - P_m(\mathbf{s}), \quad (4)$$

where $P_f(\mathbf{s})$ is a field-surveyed parameter depth or velocity and $P_m(\mathbf{s})$ is modeled depth or velocity at location \mathbf{s} . A positive error, $\epsilon(\mathbf{s}) > 0$, indicates the depth or velocity measured in the field was higher than the modeled value and water depth or velocity was underestimated. Conversely, a negative error, $\epsilon(\mathbf{s}) < 0$, indicates the field measurement was lower than the modeled value and depth or velocity was overestimated. The magnitude and spatial organization of these errors were examined using summary statistics, regression analyses, and residual maps. To assess model bias, we calculated the mean error (ME) and the mean absolute error (MAE). Similarly, we characterized model accuracy in terms of the standard deviation (SD) of the errors and the root mean square error (RMSE). We also calculated several commonly used salmon habitat metrics for each source bathymetry and compared these to measured values computed from the ADCP data. In order to examine differences between model predictions provided by each of the source bathymetries, we also compared the differences in modeled depth and velocity between the: (a) airborne hyperspectral minus the UAS hyperspectral; (b) airborne hyperspectral minus the satellite multispectral, and (c) UAS hyperspectral minus the satellite multispectral.

2.6. Habitat Models

Salmon inhabit different types of hydraulic conditions at different stages of their life history, and empirical data regarding these preferences have been used to construct suitability metrics. Mechanistic models of salmon behavior have also been used to examine salmon activities such as feeding and resting (Hafs et al., 2014; Hayes et al., 2007), as well as migration (Olivetti et al., 2021). To evaluate how different bathymetries influenced modeled salmon habitat and bioenergetic calculations, we compared predicted values of winter-run Chinook salmon spawning and rearing habitat, and adult salmon holding costs to values derived from our ADCP measurements. While we have presented two classes of habitat related metrics here for illustration, additional metrics appropriate to other fish species or forms of aquatic life could be evaluated in a similar manner.

2.6.1. Spawning Habitat

We used 2D flow simulations to quantify habitat suitability for spawning winter-run Chinook salmon. Spawning habitat quality was predicted on the basis of resource selection functions (RSF) developed for Sacramento River winter-run by Dudley et al. (2022); depth and velocity RSF are shown as blue lines in Figure 3. We used the temperature-independent RSF (Equation 3 in Dudley et al. (2022)), which calculates spawning habitat quality based on water depth and velocity using logistic regression. We used modeled depth and velocity to calculate spawning habitat RSF values between 0 and 1 for each cell of the model grid.

2.6.2. Rearing Habitat

We used 2D habitat suitability simulations to quantify winter-run Chinook salmon juvenile rearing habitat. The juvenile rearing habitat suitability model was based on depth and velocity habitat suitability curves developed in the Sacramento River for winter-run Chinook salmon (USFWS, 2005) (green dotted lines in Figures 3a and 3b). We used modeled values of depth and velocity to calculate dimensionless depth (D_{HSI}) and velocity (U_{HSI}) habitat suitability indices at each model grid cell. We then produced combined habitat suitability indices (CSI), calculated as $CSI = (D_{HSI})^{0.5}(U_{HSI})^{0.5}$, where the combined CSI predictions had values between 0 and 1, with 1 being the highest quality habitat (Gard, 2014).

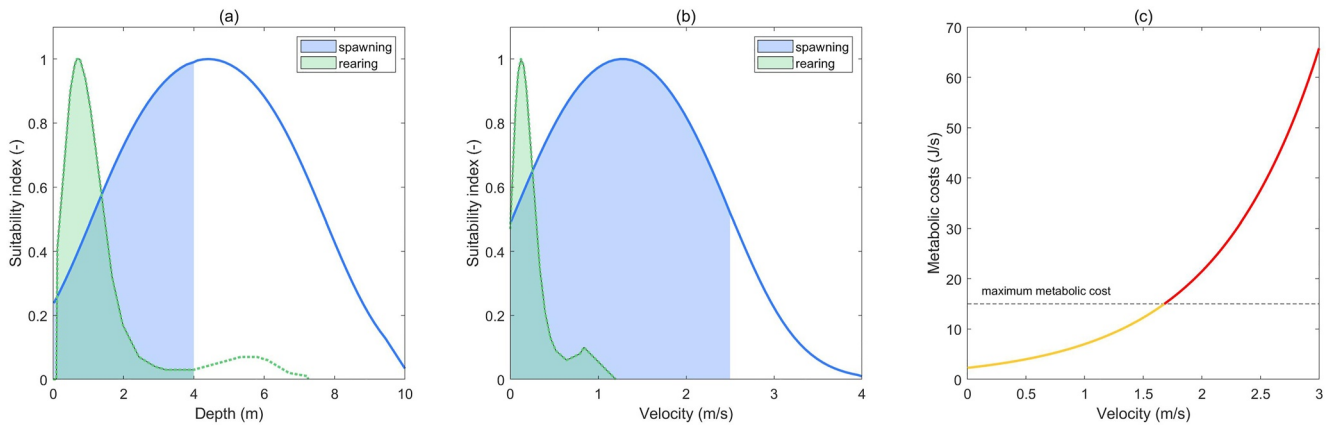


Figure 3. Winter-run Chinook salmon spawning and rearing (a) depth, (b) velocity, and (c) adult holding habitat curves. Spawning habitat preference curves were based on Dudley et al. (2022). The shading in panels (a) and (b) represent the range of measured depths and velocities present at the study site. We used a fish length of 74.6 cm (Poytress, 2016) in the metabolic holding cost estimates shown in panel (c), where the orange and red lines denote suitable and unsuitable holding velocities, respectively.

2.6.3. Holding Habitat

Adult holding costs quantify the amount of energy a fish must expend to maintain position at a given location in the river before spawning. We equate the holding cost with the metabolic rate of an adult fish while holding, which is calculated as:

$$E = \eta M^\kappa e^{\mu T} e^{\beta u}, \quad (5)$$

where E is the metabolic rate (J/d); M is the fish mass (g); T is the water temperature (12°C); u is the water velocity (m/s); and η , κ , μ , and β are parameters fitted on the basis of metabolic data. To estimate these parameters, we fit Equation 5 to metabolic rate data from five studies (Brocksen & Bailey, 1973; Cech & Myrick, 1999; Geist et al., 2003; Rombough & Ure, 1991; Thorarensen & Farrell, 2006). If length to mass conversion was necessary, we used the standard length to mass formula ($M = aL^b$) fitted with data from four studies (Chapman et al., 2013; Kimmerer et al., 2005; MacFarlane & Norton, 2002; Michel et al., 2013), where L is the fish length, and a and b are fitted parameters. Values of the fitted parameters used in this study were $\eta = 70.9$ J/d, $\kappa = 0.88$, $\mu = 0.0157$ $1/^\circ\text{C}$, and $\beta = 0.0112$ s/m.

Adult salmon can maintain position in velocities up to approximately 1.7 m/s, which can be viewed as an upper velocity limit for salmon during swimming activities (Geist et al., 2003). Based on a maximum swimming velocity of 1.7 m/s, combined with a mean fish length of 74.6 cm for winter-run Chinook salmon on the Sacramento River (Poytress, 2016), we calculated the maximum metabolic cost to be 15 J/s. We assumed that sections of the river with metabolic costs greater than 15 J/s were unsuitable for holding.

We compared habitat metrics calculated from the ADCP data to modeled habitat values to evaluate the degree to which errors in modeled depth and velocity propagated into habitat predictions. The spawning and rearing curves used in this study were developed using measurements of the total water depth, H , and depth-averaged velocity. Therefore, for the measured versus predicted spawning and rearing habitat assessment, we compared depth-averaged velocities measured by the ADCP with those predicted by 2D models. The bioenergetic holding costs can be used to relate fish energy expenditure to point velocities, which allowed us to compare the holding costs calculated from the ADCP measurements to both the 2D and 3D model-based holding cost estimates.

3. Results

3.1. Hydrodynamic Model Performance

3.1.1. Modeled Depth

We found that the water depths predicted using the 2D and 3D models were virtually identical to each other (Figure 4 and Table 2). The most accurate depths were provided by the airborne hyperspectral sensor, which had

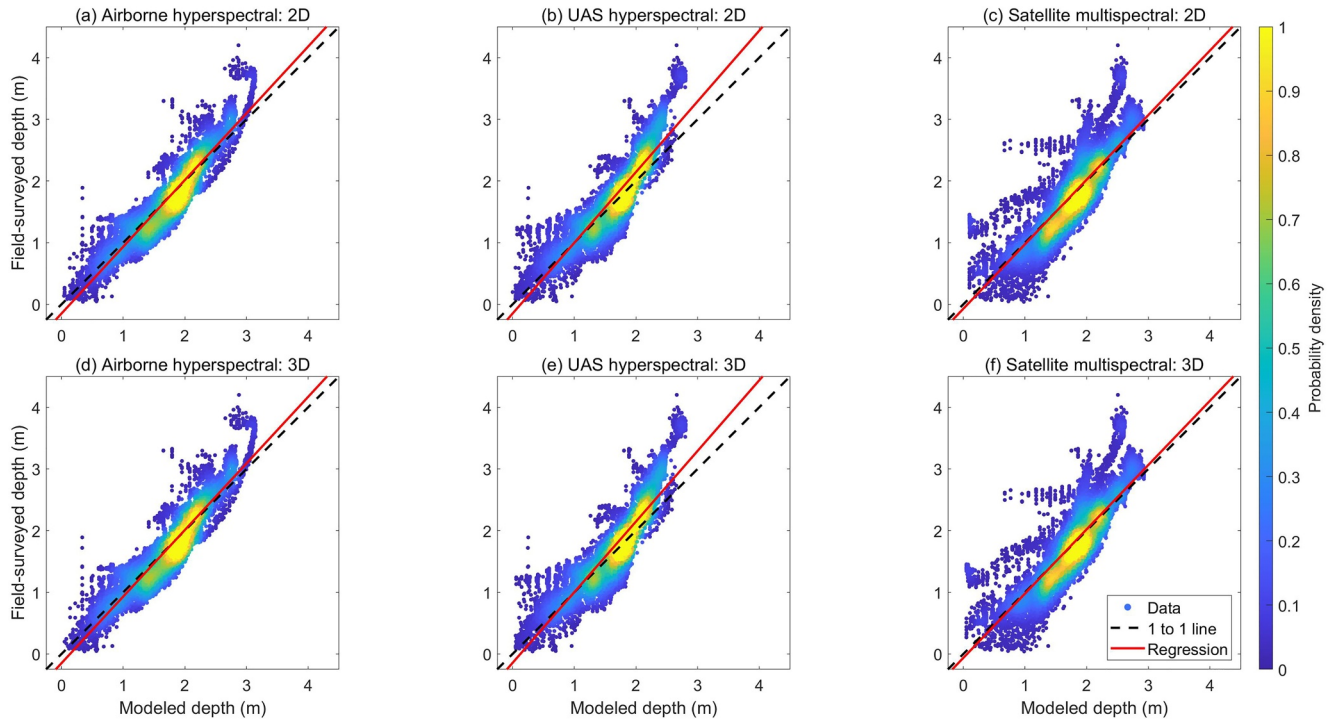


Figure 4. Measured versus modeled depth scatter plots for 2D (a–c) and 3D model simulations (d–f). The mean water depth was 1.77 m ($n = 19,024$).

2D and 3D model RMSE values of 0.24 m, equivalent to $\sim 14\%$ of the mean depth (Figures 4a and 4d). 2D and 3D model results obtained from the UAS hyperspectral bathymetry had lower accuracy, with RMSE values of 0.29 m (17% of the mean) (Figures 4b and 4e). The 2D and 3D models developed using satellite multispectral data had the lowest accuracy (RMSE = 0.35 m; 19% of the mean), with greater scatter about the regression line (Figures 4c and 4f). Each of the models tended to underestimate depths in water deeper than approximately 3 m, which accounted for $\sim 4\%$ of the measured depths. The UAS hyperspectral data had the strongest bias with a mean error of 0.1 m (6% of the mean), while models developed using the airborne hyperspectral and satellite multispectral bathymetries had mean errors close to zero ($< 1\%$ of the mean depth).

We also examined spatial patterns in observed versus predicted depths throughout the reach. Figure 5 shows the modeled depths for each of the source bathymetries. Due to the similarities in predicted depths between the 2D and 3D models, we only provide examples from 2D models for illustration; depth error summary statistics for 2D and 3D models are provided in Table 2. In general, modeled depths showed a similar spatial pattern for all three of the source bathymetries. The airborne and UAS hyperspectral data provided smoother modeled water depths, due

Sensor	Airborne hyperspectral		UAS hyperspectral		Satellite multispectral	
	2D	3D	2D	3D	2D	3D
Model	2D	3D	2D	3D	2D	3D
Mean error (%)	−0.1	−0.4	5.4	5.5	0.6	0.6
Standard deviation (%)	13.5	13.5	16.0	16.0	19.1	19.1
Mean absolute error (%)	10.4	10.5	12.2	12.3	13.6	13.6
RMSE (%)	13.5	13.5	16.9	16.9	19.1	19.1
OP R^2	0.86	0.86	0.82	0.82	0.72	0.72
OP slope	1.08	1.08	1.15	1.15	1.05	1.04
OP intercept	−0.15	−0.15	−0.15	−0.14	−0.07	−0.06

Note. OP = observed versus predicted.

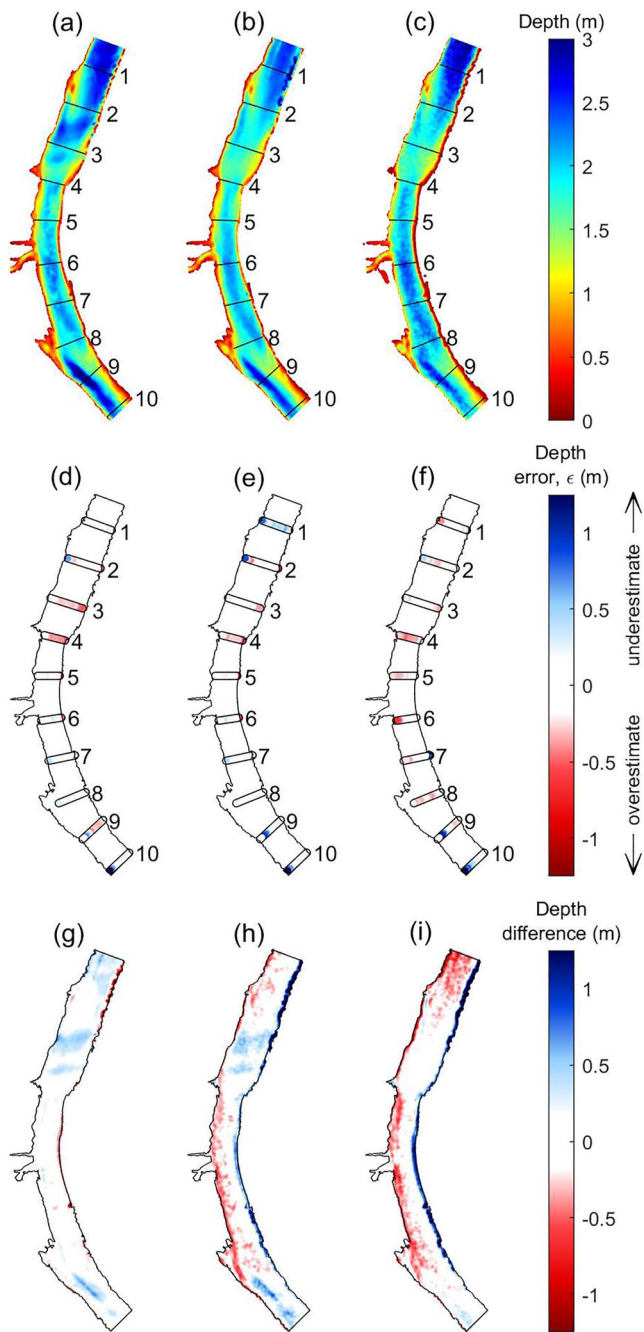


Figure 5. Predicted water depths obtained using Delft3D-FM 2D models for the (a) airborne hyperspectral, (b) UAS hyperspectral, and (c) satellite multispectral source bathymetries. Hydraulic modeling residuals, $\epsilon(s)$, calculated as field-surveyed minus modeled depths for the (d) airborne hyperspectral, (e) UAS hyperspectral, and (f) satellite multispectral data. Predicted depth difference maps for the (g) airborne minus UAS hyperspectral, (h) airborne hyperspectral minus satellite multispectral, and (i) UAS hyperspectral minus satellite multispectral data. Table 2 provides a depth error summary for both 2D and 3D models.

to the combined effects of higher spatial resolution, greater spectral detail, and possibly finer radiometric resolution, all of which led to improved depth retrieval. For the satellite multispectral images, in contrast, the depth maps were more pixelated due to the coarser spatial resolution (1.36 m), reduced spectral detail, and possibly lower radiometric resolution. Each of the models was able to capture the shallow depths occurring on the right side of the river at the upstream end of the reach between XS# 1–2 and over the shallow point bar located along the left bank near XS# 6 (Figures 5a–5c). The largest depths occurred in pools located at the upstream end of the reach (XS# 1–3) and downstream from the bend apex (XS# 8–9). The airborne hyperspectral and satellite multispectral data both captured the deeper pools while the UAS hyperspectral data tended to underestimate pool depths, particularly for the upstream pool (Figure 5).

The depth errors, $\epsilon(s)$, calculated as field-surveyed minus predicted depths, are provided in Figures 5d–5f for each of the ten cross-sections. Each of the models over-predicted water depths at XS# 4 near the channel constriction, indicated by the negative depth error shown in the red shading. Model depths were underestimated in the deepest portions of the pools located beyond the bend apex (XS# 9–10), indicated by the blue points in the depth error maps. We observed larger depth residuals near channel banks in the satellite multispectral supported model (XS# 6–7).

Maps of modeled depth differences between the airborne and UAS hyperspectral data indicated that these two source bathymetries provided similar depth predictions, with the airborne hyperspectral data leading to slightly greater pool depths, as indicated by the blue shading in Figure 5g. Similar maps representing the predicted depth difference between the airborne hyperspectral and satellite multispectral showed that the multispectral model predicted greater depths than the model based on airborne hyperspectral data in the upstream pool and along the right bank of the meander bed, highlighted by the red shading in Figure 5h. The UAS hyperspectral model predicted shallower depths than the satellite multispectral data in the upstream pool and outer bank of the meander bend, denoted by the red shading in Figure 5i.

3.1.2. Modeled Velocities

Predicted depth-averaged velocities from the 2D model are provided in Figure 6. Each of the models captured the main spatial patterns of the 2D velocity field. Similar to the modeled depths, the UAS hyperspectral provided the smoothest predicted velocities, while velocities predicted from the satellite multispectral data were noisier (Figure 6). The 2D models each predicted low velocities in the upstream pool and flow acceleration as the channel width decreases due a flow constriction near XS# 4. A high velocity jet was evident through the meander bend, with the strength of the jet diminishing with distance downstream from the constriction. Low velocities occurred along the channel margins, near the confluence with Cottonwood Creek, and in a small alcove located on the right side of the river downstream from the bend apex near XS# 8 (Figures 6a–6c).

We found that errors, $\epsilon(s)$, between field-surveyed and predicted velocities were generally small, as indicated by the white shading in the velocity error plots (Figures 6d–6f). The most notable discrepancy between measured and modeled depth-averaged velocities was the underestimation of velocities near the channel constriction for all sensors, shown as blue colors in the velocity error plots at XS# 4 (Figures 6d–6f). The UAS hyperspectral and satellite multispectral data slightly overestimated velocities in the downstream end of the reach, indicated by red colors in the velocity error maps at XS# 9

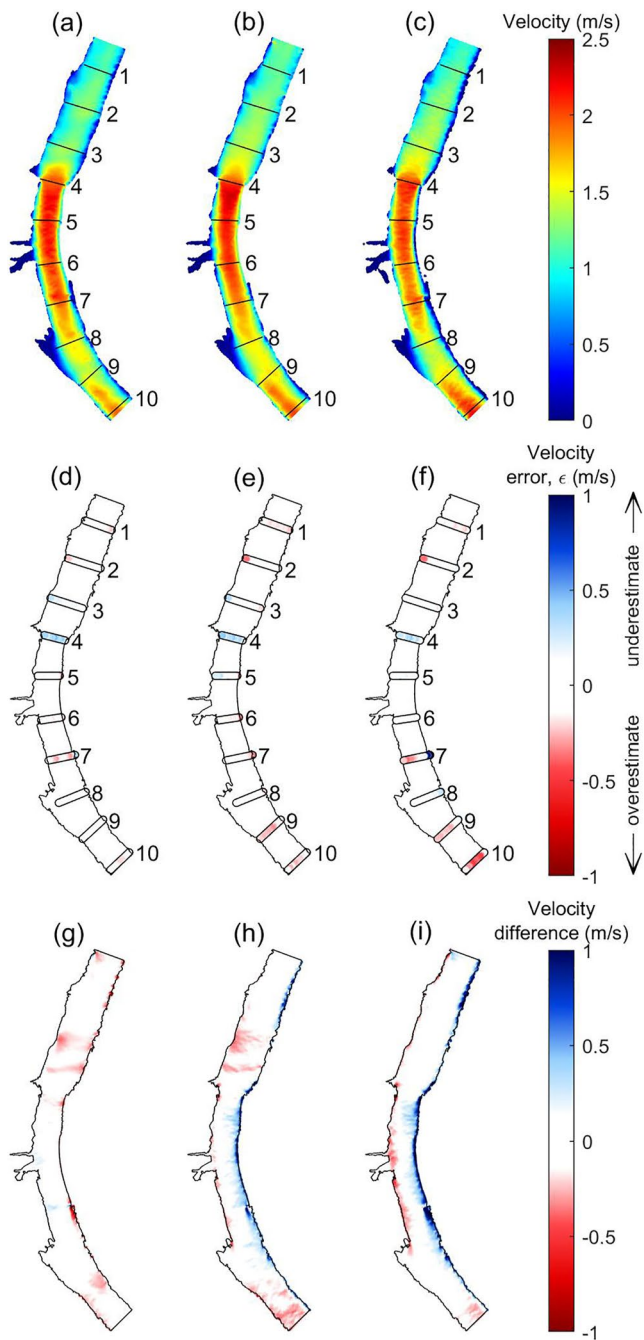


Figure 6. Predicted depth-averaged velocities obtained using Delft3D-FM 2D models for the (a) airborne hyperspectral, (b) UAS hyperspectral, and (c) satellite multispectral source bathymetries. Hydraulic modeling residuals, ϵ (s), calculated as field-surveyed minus modeled depth-averaged velocities for the (d) airborne hyperspectral, (e) UAS hyperspectral, and (f) satellite multispectral data. Predicted velocity difference maps for the (g) airborne minus UAS hyperspectral, (h) airborne hyperspectral minus satellite multispectral, and (i) UAS hyperspectral minus satellite multispectral data. Table 3 provides a velocity error summary for both 2D and 3D models.

and 10. The model developed using satellite multispectral data also underestimated velocities near the left bank at XS# 7, shown in dark blue colors in the velocity error plot (Figure 6f).

Maps illustrating the difference between velocities modeled based on the airborne and UAS hyperspectral data indicated that the source bathymetries generally provided similar velocity predictions, with the airborne hyperspectral data leading to slightly lower velocities (red shading in Figure 6g). Similarly, calculating the differences between velocity predictions based on the airborne hyperspectral and satellite multispectral showed that the model predicted slower velocities when using bathymetry derived from airborne hyperspectral data than when using the multispectral satellite data as input, particularly in the upstream and downstream pools (red shading in Figure 6h). Conversely, the blue shading in Figure 6h represents faster velocities from the airborne hyperspectral data compared to the satellite multispectral model along the point bar. The UAS hyperspectral predicted faster velocities than the satellite multispectral data along the point bar, denoted by the blue shading in Figure 6i.

We found generally good agreement between velocity magnitudes measured with an ADCP and those predicted with the 3D models (Figure 7). The airborne hyperspectral and UAS hyperspectral data were generally able to reproduce the vertical and cross-stream velocity variations and the location of the high velocity core (XS# 4, 6, and 8). The satellite multispectral data captured the main features of the velocity field but tended to underestimate velocities near the banks. Because neither the 2D nor the 3D RANS models resolve all scales of motion present within the flow, both models predicted flow fields that were smoother than those measured directly in the field. In addition, each of the models underestimated velocities at XS# 4, where the ADCP recorded velocities greater than 2 m/s throughout the majority of the water column (Figure 7b), while the 3D models tended to predict a more gradual velocity gradient with distance from the water surface down to the riverbed at this transect location (Figure 7f, 7j, and 7n).

Our results indicated that depth-averaged velocity errors were similar between the 2D and 3D models (Table 3). The depth-averaged velocity RMSE values ranged from 11% to 16% of the mean velocity for the airborne hyperspectral, UAS hyperspectral, and satellite multispectral, respectively. The R^2 values were between 0.81 and 0.86 for the airborne hyperspectral and UAS hyperspectral data, whereas the satellite multispectral data led to R^2 values of 0.72 and 0.73 for the 2D and 3D models, respectively.

The RMSE values for the near-bed velocity errors were similar between the 2D and 3D models, with values between 14% and 17% of the mean near-bed velocity for the airborne hyperspectral and UAS hyperspectral data and between 20% and 21% of the mean near-bed velocity for the satellite multispectral data. While the standard deviation and RMSE values were similar for near-bed velocity errors provided by 2D and 3D models, the 3D models tended to have less bias in the near-bed velocity predictions, with values between -3 and 2% of the mean near-bed velocity, compared to mean errors of 7% – 10% of the mean near-bed velocity for the 2D models. The R^2 between measured and predicted near-bed velocities were between 0.77 and 0.81 for the 2D and 3D airborne hyperspectral and UAS hyperspectral models, while the satellite multispectral data had R^2 between 0.63 and 0.69 for the 2D and 3D models.

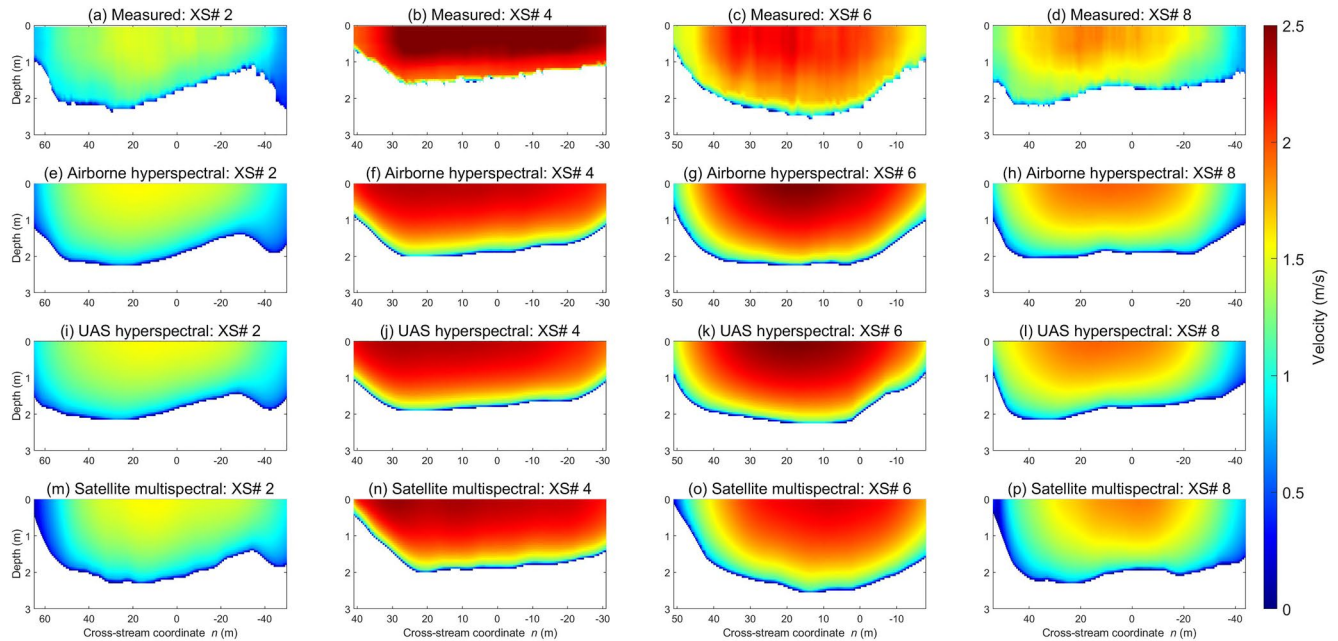


Figure 7. Measured and modeled 3D velocities for cross-sections # 2, 4, 6, and 8. The view is downstream and the cross-stream coordinate n is referenced to the centerline ($n = 0$), with larger negative (positive) values toward the right (left) bank. The location of each transect is provided in Figure 1.

3.2. Modeled Salmon Habitat

Predicted values provided by 2D models of winter-run Chinook salmon spawning, juvenile rearing, and holding habitats are shown in Figure 8. The spatial patterns of 2D modeled spawning habitat were similar between the three source bathymetries, with high-quality spawning habitat predicted in deep pools at both the upstream end

Table 3
Modeled Velocity Error Summary Statistics

Sensor	Airborne hyperspectral		UAS hyperspectral		Satellite multispectral	
	2D	3D	2D	3D	2D	3D
Depth-averaged velocity (m/s)						
Mean error (%)	-0.8	-2.3	-4.7	-2.8	-1.9	1.6
Standard deviation (%)	10.6	10.8	11.3	12.4	15.2	15.7
Mean absolute error (%)	8.4	8.9	10.0	10.1	11.4	11.9
RMSE (%)	10.7	11.1	12.2	12.7	15.3	15.8
OP R^2	0.86	0.86	0.84	0.81	0.73	0.72
OP slope	0.97	0.95	1.04	0.96	0.86	0.84
OP intercept	0.03	0.05	-0.13	0.02	0.18	0.25
Near-bed velocity (m/s)						
Mean error (%)	9.5	0.9	6.9	-2.5	9.1	2.0
Standard deviation (%)	14.1	14.3	15.6	14.2	17.5	20.4
Mean absolute error (%)	12.5	10.7	12.7	11.3	14.9	15.4
RMSE (%)	17.0	14.4	17.0	14.4	19.7	20.5
OP R^2	0.81	0.80	0.77	0.80	0.69	0.63
OP slope	1.14	0.95	1.19	1.00	1.02	0.79
OP intercept	-0.03	0.06	-0.09	-0.03	0.07	0.21

Note. Reach-averaged values of depth-averaged and near-bed velocities are 1.44 and 0.94 m/s, respectively.

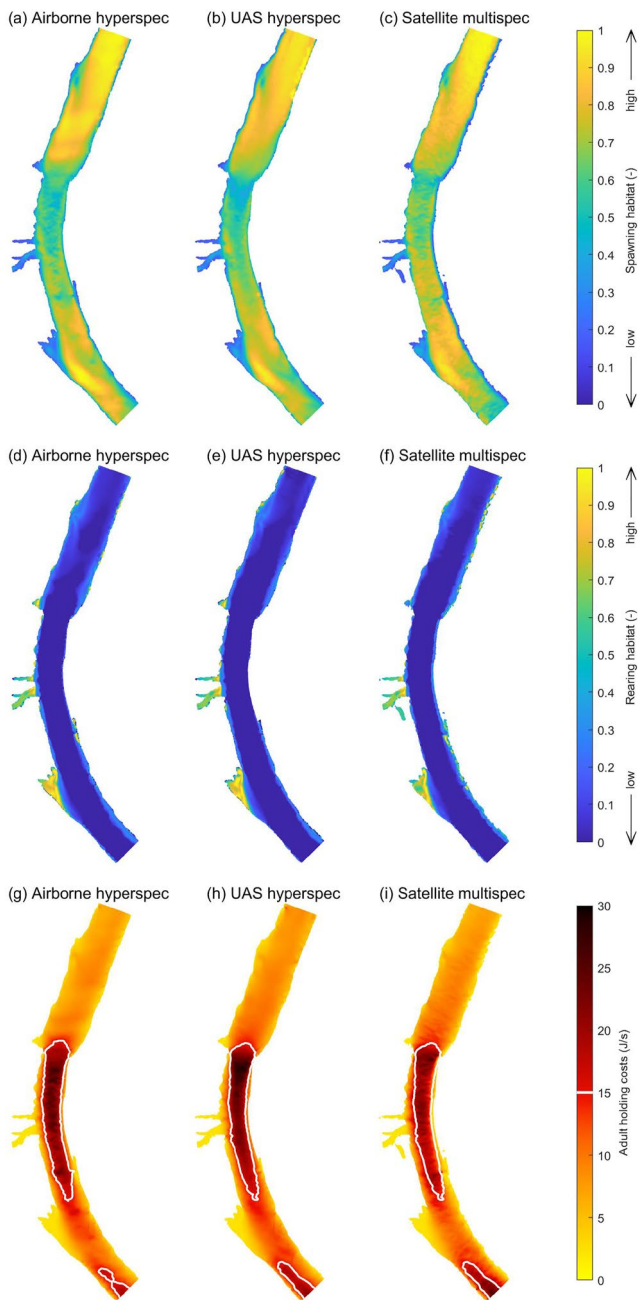


Figure 8. Modeled 2D salmon (a–c) spawning habitat, (d–f) rearing habitat, and (g–i) metabolic holding costs. White contour lines in panels g–i represent areas predicted to exceed the maximum aerobic energy expenditure (15 J/s) of holding adults.

of the reach and downstream from the bend apex. These pools had depths typically greater than 1 m and velocities between 1 and 1.5 m/s, resulting in dimensionless spawning habitat quality values greater than 0.7, as indicated by the yellow and orange shading in Figures 8a–8c. Lower quality spawning habitat, shown in cool colors, occurred through the channel constriction where the flow was shallower and faster, with velocities in excess of 2 m/s. The slow-shallow channel margins and confluence region were also predicted to provide low-quality spawning habitat, represented by the blue shading in Figures 8a–8c.

High-quality juvenile rearing habitat predicted from 2D models was located in a backwater on the right bank downstream from the bend apex (Figures 8d–8f). This alcove had water depths less than 1 m and depth-averaged velocities below 0.15 m/s, resulting in modeled rearing *CSI* values greater than 0.7, indicated by the warm colors in Figures 8d–8f. Medium to high-quality juvenile rearing habitat was predicted near the confluence with Cottonwood Creek, indicated by the green and yellow shading in Figures 8d–8f. Very narrow zones of medium quality juvenile rearing habitat (*CSI* > 0.5) were predicted along channel margins, while the main river channel was predicted to provide low quality rearing habitat (cool colors in Figures 8d–8f), due to depth-averaged velocities in excess of 0.15 m/s throughout the majority of the mainstem channel.

The 2D modeled metabolic rates for fish holding (*E*) were predicted to be suitable for the majority of the pool habitats, as indicated by the orange colors in Figures 8g–8i. The channel constriction zone was predicted to be largely unsuitable as energy expenditures were predicted to exceed 15 J/s, indicated by the red and dark shading in Figures 8g–8i. The spatial extent of unsuitable holding habitat (white polygon in Figures 8g–8i) was similar between the three source bathymetries, though peak values of *E* were greatest for the UAS hyperspectral data. A small region of unsuitable holding habitat was also predicted near the downstream end of the reach, with the satellite multispectral and UAS hyperspectral data predicting slightly larger unsuitable areas in this region compared to the airborne hyperspectral data.

The areal extent of 2D modeled spawning, juvenile rearing, and adult holding habitat was similar across the three source bathymetries (Figures 9a–9c). The airborne hyperspectral, UAS hyperspectral, and satellite multispectral models predicted that 56%, 55%, and 61% of the total area provided high-quality spawning habitat (>0.7). The airborne hyperspectral, UAS hyperspectral, and satellite multispectral models predicted that 3%, 3%, and 2% of the total area provided high-quality juvenile rearing habitat. The three models predicted that between 79% and 80% of the reach provided suitable holding habitat (<15 J/s).

The 2D modeled spawning habitat predictions had low errors with the majority of errors within ± 0.1 (Figure 9d). The airborne hyperspectral and UAS hyperspectral had the narrowest error distributions, while the multispectral satellite data had slightly larger spawning habitat errors. The juvenile rearing

habitat errors were close to zero for all three sensors (Figure 9e). Holding cost errors were generally small for the airborne hyperspectral and UAS hyperspectral data, while the multispectral satellite had an error distribution with greater spread (Figure 9f). Note that while absolute values of the holding cost errors were larger than the spawning and rearing habitat errors (Figures 9d–9f), the spatial extent of suitable holding habitat (<15 J/s) was virtually identical across the three source bathymetries (Figures 8g–8i).

Figure 10 provides a comparison between measured and modeled 3D metabolic holding costs at cross-sections #2, 4, 6, and 8. Each of the source bathymetries predicted suitable holding habitat throughout the full water

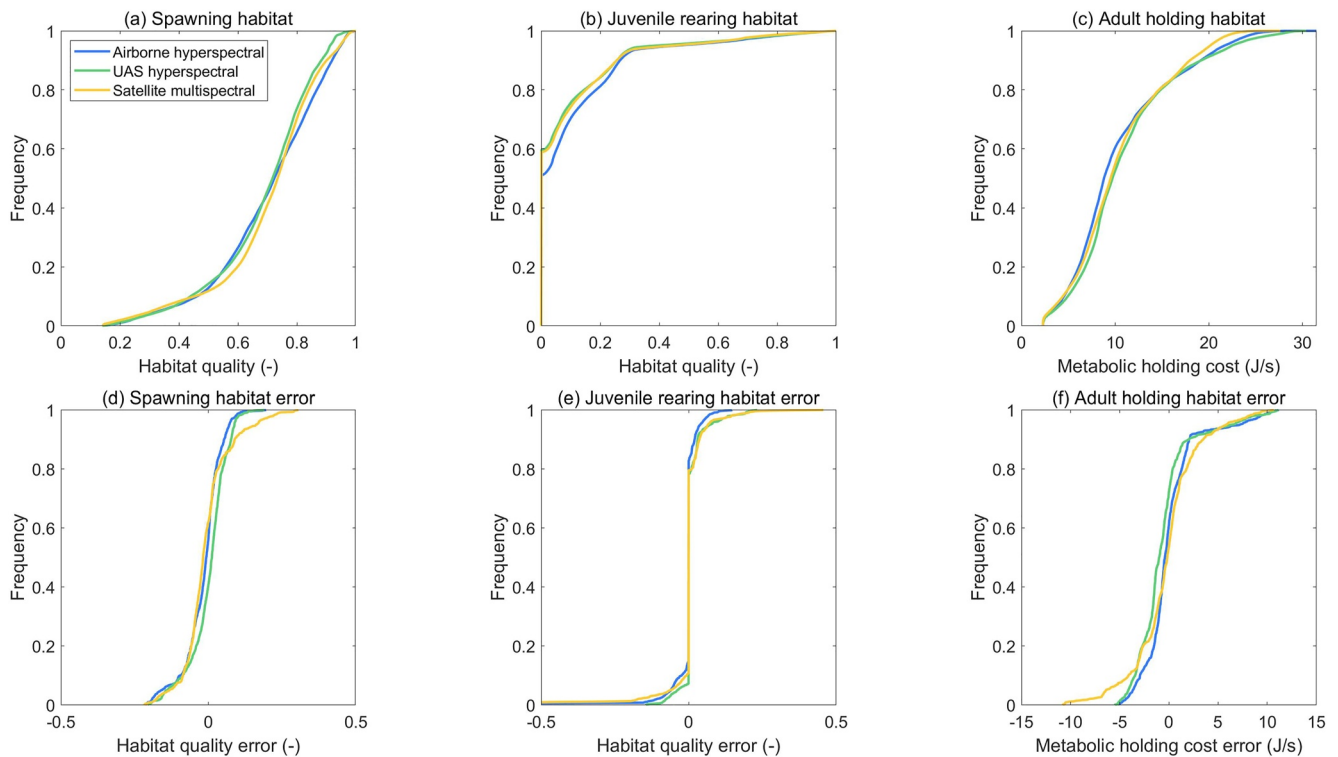


Figure 9. Cumulative frequency distributions for spawning, holding and rearing habitat quality (a–c) and errors (d–f) predicted from 2D models.

column in the upstream pool at XS #2, consistent with values obtained from the ADCP. Measured metabolic holding costs at the constriction (XS #4) exceeded 15 J/s throughout most of the flow depth, with just a thin layer of suitable holding habitat near the channel bed. Modeled holding costs at XS #4 predicted a thickness of unsuitable holding habitat similar to that measured in the field, but the models estimated a thicker layer of suitable

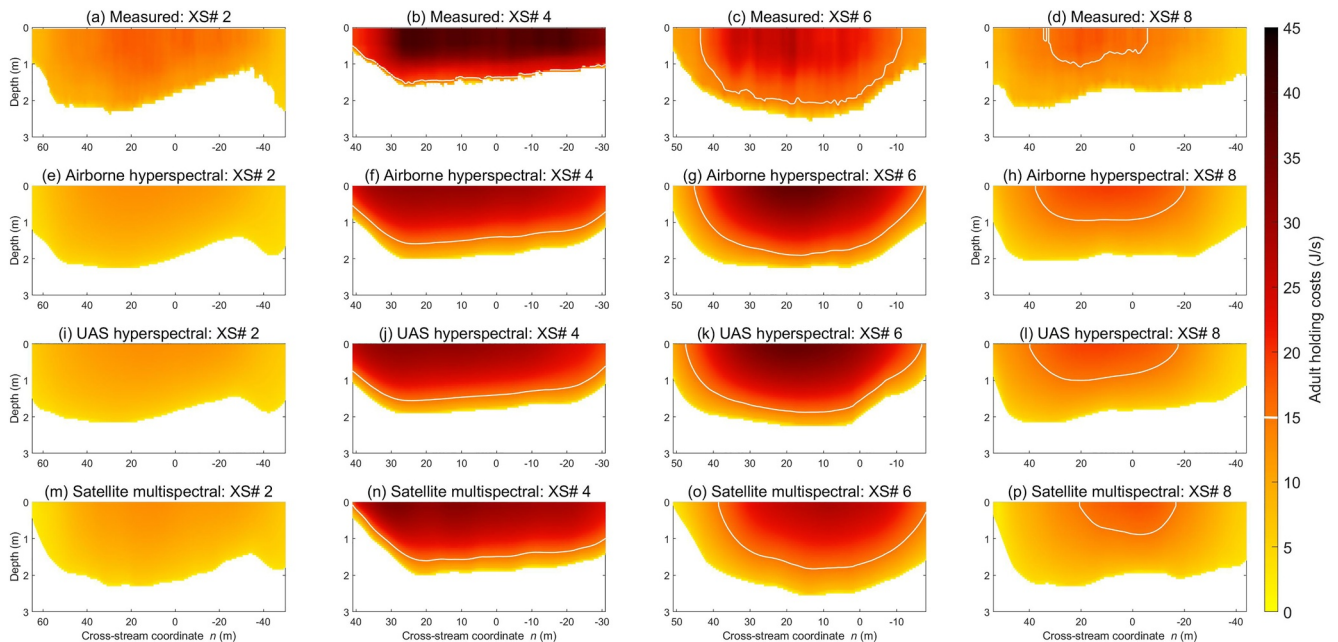


Figure 10. Comparison between measured and modeled 3D adult holding costs for cross-sections # 2, 4, 6, and 8. Areas above the white contour lines are predicted to exceed the maximum energy expenditure (15 J/s) of holding adults.

holding habitat in the lower portion of the water column. The spatial pattern of holding costs was similar between the ADCP and modeled values near the meander bend apex (XS #6) and downstream pool (XS #8).

4. Discussion

4.1. Ecohydraulic Model Sensitivity to Remotely Sensed River Bathymetry

Our study provided the first evaluation of the potential for developing 2D and 3D computational fluid dynamics (CFD) models for a large, gravel-bed river using multiple, passive optical remotely sensed river bathymetries as model input. Our model accuracy assessment found that predicted water depth errors (RMSE) ranged from 14% to 19% of the mean depth, and R^2 values ranged from 0.72 to 0.86 (Table 2). Previous studies have reported 2D and 3D model errors generally below 20% of the mean depth or velocity and have R^2 values greater than 0.8 (Tonina & Jorde, 2013). Using these benchmark values, the airborne hyperspectral and UAS hyperspectral source bathymetries satisfied accepted model validation standards, while the models developed from satellite multispectral data provided lower accuracy predictions than previously published multi-dimensional modeling studies. The satellite multispectral imagery had lower spectral and spatial resolution than the airborne hyperspectral and UAS hyperspectral imagery, which created a more pixelated source bathymetry and contributed to larger bathymetric errors (Legleiter & Harrison, 2019a). Based on our evaluation of the three source bathymetries, we concluded that for rivers of similar width, depth, and clarity to the reach of the Sacramento River we examined, hyperspectral sensors, whether deployed from piloted aircraft or UAS, appeared to have greater potential for parameterizing multi-dimensional flow models than the satellite multispectral imagery.

We found that errors in modeled water depth were comparable to the uncertainty in the input source bathymetry. Legleiter and Harrison (2019a) reported depth error standard deviations of 14%, 15%, and 18% of the mean depth for the airborne hyperspectral, UAS hyperspectral, and satellite multispectral sensors, respectively. Using those same bathymetries as 2D and 3D model input, we observed modeled depth error standard deviations of ~14%, 16%, and 19% of the mean depth. Thus, the uncertainty in the image-based depth maps can provide a first-order estimate of the depth errors to be expected when using the remotely sensed bathymetry as input for multi-dimensional flow models. In a study of shallow, braided river flow dynamics, Javernick et al. (2016) found 2D model depth errors of similar magnitude to the input bathymetric DEM they derived from optical imagery, consistent with our results for 2D and 3D models developed for a large river.

Our study suggested that the fine-scale microtopography captured by high resolution bathymetric data could be incorporated into the input DEMs used for hydraulic model development. Although Delft3D-FM does not include sub-element topography smaller than the grid dimensions (1 m² in this study), the high-resolution DEMs could partially account for form drag and thus require lower flow resistance values than many previously published studies. In a compilation of roughness height, k_s , values from the literature, García (2008) reported α_s values of 2–3, whereas we found that an $\alpha_s \approx 1.2$ provided the best agreement between measured and modeled depths. Previous multi-dimensional flow modeling studies using high resolution topography have obtained α_s values in the range of 0.9–1.4 (Williams et al., 2013). Tonina et al. (2020) also report that high resolution topography captures much of the roughness of the streambed, thus requiring lower flow resistance values in 2D model development, which in their case were assigned using values of the Manning's n coefficient. Results from our study, in conjunction with previous modeling studies (Tonina et al., 2020; Williams et al., 2013), can be used to inform flow resistance parameterization in future modeling investigations using high resolution topo-bathymetric data. Our findings, in conjunction with previous work (Tonina et al., 2020; Williams et al., 2013), imply that as high-resolution topo-bathymetric datasets become more widely used to develop multi-dimensional flow models, conventional methods of estimating roughness values might need to be reevaluated.

Our results indicate that measured and modeled velocity fields were generally in good agreement, with errors of similar magnitude to previous modeling studies. Consistent with the results of our depth accuracy assessment, the airborne hyperspectral data provided the most accurate velocity predictions, followed by the UAS hyperspectral and satellite multispectral data. Model errors for depth-averaged velocities were similar between the 2D and 3D models, with a level of precision within the range of previously reported RMSE values, which are generally between 20% and 30% of the mean depth-averaged velocity (Pasternack & Senter, 2011). Regression analyses indicated that R^2 values for the depth-averaged velocities ranged from 0.81 to 0.86 for the airborne and UAS hyperspectral data but were less than 0.8 for the satellite multispectral data. By this metric, the model based on

satellite multispectral-derived bathymetry did not predict velocity as well as previous multi-dimensional modeling applications. The poorer performance of models developed from satellite multispectral data was likely due to georeferencing issues, which were most evident near the channel margins. Near-bed velocities had similar RMSE values between 2D and 3D models, but the 3D models had less bias (i.e., mean errors smaller in magnitude) compared to measured near-bed velocities. These results are consistent with previous studies which found that 3D models outperformed 2D models in predictions of near-bed velocities (Kasvi et al., 2015; Lane et al., 1999).

We found that the most notable discrepancy between measured and modeled velocities occurred near the width constriction. Previous studies using image-based bathymetry to parameterize 2D models reported that the largest velocity errors occurred in shallow flows in braided anabranches with depths <0.25 m (Williams et al., 2013). McKean et al. (2014) and Tonina et al. (2020) also found higher velocity errors in shallow, fast riffles than in deeper areas with plane bed and pool morphologies when using 2D models developed from bathymetric lidar DEMs. While results from our study are generally consistent with previous work on small to medium-sized rivers using 2D models (McKean et al., 2014; Tonina et al., 2020; Williams et al., 2013), we observed the largest velocity errors in fast, deep run habitats, which are more common than fast, shallow riffle habitat on the Sacramento River. Although we did observe some discrepancies between measured and modeled flow fields, the source bathymetries we used had relatively small vertical errors overall. Therefore, some of the model error could also be attributed to inherent limitations of the 2D and 3D models and other aspects of their parameterization.

Modeled spawning and juvenile rearing habitat indices had low errors for each of the three sensors (Figure 9), despite observed errors in modeled depth and velocity. For example, the tendency of each of the models to underestimate the maximum pool depths did not have significant impacts on the spawning or rearing habitat quality predictions (Figure 8). This result could reflect the specific habitat requirements of winter-run Chinook salmon that spawn in deeper water than other salmon (Moyle et al., 2017), such as fall-run Chinook salmon, who typically spawn in shallow, fast transition zones between pools and riffles (Harrison et al., 2019). Juvenile winter-run Chinook salmon prefer slow (<0.15 m/s) water approximately 1 m deep (USFWS, 2005), such as the channel alcove located beyond the bend apex in our study reach. In this location, each of the models predicted a continuous patch of medium to high-quality habitat, demonstrating consistency between juvenile rearing habitat predictions provided by the three source bathymetries (Figure 8). Habitat suitability assessments for other species will vary depending on channel characteristics and species habitat preferences; results from other rivers thus could differ from those we obtained.

Predicted bioenergetic holding costs are calculated as a function of velocity and we found that modeled holding costs were sensitive to velocity errors (Figure 9f). The UAS hyperspectral and satellite multispectral data overestimated velocity in the lower portion of the reach near XS# 9–10 (Figure 6), resulting in a corresponding over-prediction of metabolic holding costs in this region (Figures 8h and 8i). Swimming migration costs, similar to holding costs, are often used to calculate the total energy expenditure of adult salmon from the beginning of upstream migration until spawning (Connor et al., 2019; Lennox et al., 2018). Potential migration cost errors could be significant when calculating the energy reserves remaining when the salmon reach their spawning grounds, which would affect efforts to model the amount of time a Chinook salmon could defend a redd and thus affect estimates of redd superimposition in spawning grounds. Our 3D modeling illustrated that metabolic costs varied with distance from the bed, and suitable holding habitat existed near the river bed even in swiftly moving river sections. The added vertical dimension provided by the 3D models is a clear advantage over 2D approaches for visualizing and quantifying species-habitat interactions and yields a more complete representation of the conditions experienced by migrating and holding fish.

4.2. Practical Considerations in Using Remotely Sensed Bathymetry in Hydraulic Modeling Studies

Our study had several important limitations. For this study, we modeled a single discharge of 260 m³/s, the flow observed during our field and remote sensing campaigns, which occurred at a time when we could safely wade the shallow margins of the channel and operate a jet boat within the Sacramento River. The discharge we simulated was approximately 80%, 104%, and 94% of the estimated spawning, rearing, and holding flows experienced by winter-run Chinook salmon on the Sacramento River. While collecting additional hydraulic measurements at higher discharges would have been preferable, this was not feasible on the Sacramento River due to safety concerns for field personnel. Nevertheless, we acknowledge that predicted depths, velocities, and habitat metrics will differ for other discharges.

Our study used spatially variable flow resistance values in the models, which were based on a single k_s value and local water depths (see Equation 2). The use of a single k_s value was necessitated by a lack of continuous sediment grain-size data, which in the case of the Sacramento River, would have required detailed sediment sampling using a boat and dredge or similar sampler (Singer, 2008), which was beyond the scope of this study. Sediment patches can have a strong effect on the flow field (Nelson et al., 2015), most notably in the increased (decreased) velocities that can be associated with fine (coarse) sediment grains (Tonina et al., 2020). By using a single k_s value, our modeling does not capture such small-scale flow variations induced by sediment patches. However, because the k_s value was the same for each of the three model bathymetries, any errors introduced by not including spatially variable sediment grain sizes would have affected models developed from each of the three bathymetries and presumably in a similar manner. Furthermore, because including sediment patch information would likely improve velocity predictions, our model estimates provide a conservative estimate of the predictive capability that can be achieved in the more typical situation where spatially explicit grain size data are not available. Remote sensing methods for mapping continuous sediment grain size data using airborne lidar (Chardon et al., 2020) and UAS-based imagery (Woodget et al., 2018) offer a potential means for developing continuous grain size estimates on exposed gravel bars along large rivers. Methods for mapping submerged substrates using multibeam acoustic backscatter data (Buscombe et al., 2017) could provide an additional method of characterizing continuous bed sediment grain sizes on large rivers for the purpose of parameterizing 2D/3D models.

We found that the maximum detectable depth in the image-derived bathymetry imposed an important constraint on the accuracy of predicted depths obtained using 2D and 3D numerical models. All three of the source bathymetries underestimated the maximum pool depths beyond the bend apex, where depths exceeded 3 m (Figure 3). This 3 m threshold was exceeded by only 4% of the water depths we measured directly in the field. This result highlights the potential limitations for using image-based bathymetric DEMs to develop multi-dimensional flow models on large rivers. Passive optical methods may provide limited depth information in turbid, deep water, which would present an additional challenge for using image-based bathymetric DEMs as input for multi-dimensional flow models on large rivers. To overcome these limitations, a hybrid approach using multibeam echo sounders (MBES) in conjunction with remotely sensed bathymetry could provide a feasible alternative to relying solely on remotely sensed data for model development. Legleiter and Fosness (2019) developed an approach for identifying areas exceeding the maximum detectable depth within an image, which could help to improve image-based bathymetric DEM generation. Once the maximum depth is identified, field sampling strategies could be developed to fill in voids where image-based methods do not provide accurate depths. This type of hybrid approach is common on large rivers where bathymetric lidar data is supplemented with MBES data to fill in voids found in deeper water (Yurok Tribe, 2018), and a similar strategy could be adopted for passive optical approaches to mapping river bathymetry on large rivers for the purpose of constructing DEMs suitable for flow modeling.

Our study demonstrated the potential for using remotely-sensed bathymetry to develop multi-dimensional flow models for a 1.6 km reach of a large river. Although our results are encouraging, the potential for developing ecohydraulic models using remotely-sensed bathymetry at larger spatial scales has not been demonstrated. Of the three sources we evaluated, the airborne hyperspectral sensor appears most suitable for larger-scale model applications, due to the greater depth mapping accuracy and ability to cover large spatial extents using conventional, piloted aircraft. While the UAS hyperspectral data provided accurate hydraulic and habitat quality predictions, this platform is most suitable for reach-scale applications on the order of several km. The satellite multispectral sensor has the potential to scale results up to larger spatial extents, though in our evaluation the resulting model predictions did not meet established benchmarks of hydraulic model performance. Scaling up results from reach-scale model applications to longer river segments could advance understanding of aquatic ecosystem processes at the riverscape scale (Carbonneau et al., 2012; Fausch et al., 2002; Torgersen et al., 2022).

5. Conclusion

Numerical models are fundamental tools in basic and applied ecohydraulic investigations, but improved techniques are needed to increase the efficiency of two-dimensional (2D) and three-dimensional (3D) model construction across a broad range of applications. This study evaluated the potential to develop multi-dimensional numerical models for a large, gravel-bed river using three different remotely sensed river bathymetries as model input. We found that flow resistance values obtained during model calibration were lower than previously reported in the literature, perhaps as a result of the high resolution input bathymetry we derived from remotely sensed data.

Water depth errors in 2D and 3D models were similar to one another and were comparable to the uncertainty in the input source bathymetry. We observed generally good agreement between measured velocities and those predicted using 2D and 3D models. Predicted values of winter-run Chinook salmon (*Oncorhynchus tshawytscha*) spawning and rearing habitat were similar across the three source bathymetries we evaluated, whereas bioenergetic predictions related to adult salmon holding habitat were more sensitive to velocity errors between the different bathymetric source DEMs. Our findings from the Sacramento River indicated that hyperspectral imagery acquired from piloted and uncrewed aircraft was more suitable than multispectral satellite imagery for use as bathymetric input for multi-dimensional flow models.

Data Availability Statement

The data supporting the analyses and results presented in this paper are publicly available and can be found in (Legleiter & Harrison, 2019b, 2022).

Acknowledgments

We would like to acknowledge the NOAA UAS Program Office for supporting this research. Funding for the lidar and CASI hyperspectral image data was provided by the California Department of Fish and Wildlife (Grant P1610802). Brandon Sansom provided helpful comments on an earlier draft of the paper. Bert Jagers provided valuable insight on the Delft3D-FM model. Charles Kepler, Jeremy Notch, Matt Pickett, Brian Taggart, and Alicia Amerson assisted with field and UAS data collection. Any use of trade, firm, or product names is for descriptive purposes only and does not imply endorsement by the U.S. Government.

References

- Barrera Crespo, P. D., Mosselman, E., Giardino, A., Becker, A., Ottevanger, W., Nabi, M., & Arias-Hidalgo, M. (2019). Sediment budget analysis of the Guayas River using a process-based model. *Hydrology and Earth System Sciences*, 23(6), 2763–2778. <https://doi.org/10.5194/hess-23-2763-2019>
- Benjankar, R., Tonina, D., McKean, J. A., Sohrabi, M. M., Chen, Q., & Videgar, D. (2018). Dam operations may improve aquatic habitat and offset negative effects of climate change. *Journal of Environmental Management*, 213, 126–134. <https://doi.org/10.1016/j.jenvman.2018.02.066>
- Benjankar, R., Tonina, D., McKean, J. A., Sohrabi, M. M., Chen, Q., & Videgar, D. (2019). An ecohydraulics virtual watershed: Integrating physical and biological variables to quantify aquatic habitat quality. *Ecohydrology*, 12(2), e2062. <https://doi.org/10.1002/eco.2062>
- Brocksen, R. W., & Bailey, H. T. (1973). Respiratory response of juvenile Chinook salmon and striped bass exposed to benzene, a water-soluble component of crude oil. *International Oil Spill Conference Proceedings, 1973*(1), 783–791. <https://doi.org/10.7901/2169-3358-1973-1-783>
- Brown, R. A. (2022). Hydrogeomorphic scaling and ecohydraulics for designing rescaled channel and floodplain geometry in regulated gravel-cobble bed rivers for Pacific salmon habitat. *Water*, 14(4), 670. <https://doi.org/10.3390/w14040670>
- Brown, R. A., & Pasternack, G. B. (2009). Comparison of methods for analysing salmon habitat rehabilitation designs for regulated rivers. *River Research and Applications*, 25(6), 745–772. <https://doi.org/10.1002/rra.1189>
- Buscombe, D., Grams, P. E., & Kaplinski, M. A. (2017). Compositional signatures in acoustic backscatter over vegetated and unvegetated mixed sand-gravel riverbeds. *Journal of Geophysical Research: Earth Surface*, 122(10), 1771–1793. <https://doi.org/10.1002/2017JF004302>
- Carbonneau, P., Fonstad, M. A., Marcus, W. A., & Dugdale, S. J. (2012). Making riverscapes real. *Geomorphology*, 137(1), 74–86. <https://doi.org/10.1016/j.geomorph.2010.09.030>
- Cech, J. J., & Myrick, C. A. (1999). *Steelhead and Chinook salmon bioenergetics: Temperature, ration, and genetic effects*. University of California Water Resources Center. Retrieved from <https://escholarship.org/uc/item/86z2n9wm>
- Chapman, E. D., Hearn, A. R., Michel, C. J., Ammann, A. J., Lindley, S. T., Thomas, M. J., et al. (2013). Diel movements of out-migrating Chinook salmon (*Oncorhynchus tshawytscha*) and steelhead trout (*Oncorhynchus mykiss*) smolts in the Sacramento/San Joaquin watershed. *Environmental Biology of Fishes*, 96(2–3), 273–286. <https://doi.org/10.1007/s10641-012-0001-x>
- Chardon, V., Schmitt, L., Piégay, H., & Lague, D. (2020). Use of terrestrial photosieving and airborne topographic LiDAR to assess bed grain size in large rivers: A study on the Rhine River. *Earth Surface Processes and Landforms*, 45(10), 2314–2330. <https://doi.org/10.1002/esp.4882>
- Connor, W. P., Tiffan, K. F., Chandler, J. A., Rondorf, D. W., Arnsberg, B. D., & Anderson, K. C. (2019). Upstream migration and spawning success of Chinook salmon in a highly developed, seasonally warm river system. *Reviews in Fisheries Science & Aquaculture*, 27(1), 1–50. <https://doi.org/10.1080/23308249.2018.1477736>
- Crozier, L. G., McClure, M. M., Beechie, T., Bograd, S. J., Boughton, D. A., Carr, M., et al. (2019). Climate vulnerability assessment for Pacific salmon and steelhead in the California current large marine ecosystem. *PLoS One*, 14(7), 1–49. <https://doi.org/10.1371/journal.pone.0217711>
- Deltares. (2022). *Delft3D Flexible Mesh Suite User Manual*. Retrieved from <https://www.deltares.nl/en/software/delft3d-flexible-mesh-suite/>
- Dietrich, J. T. (2017). Bathymetric structure-from-motion: Extracting shallow stream bathymetry from multi-view stereo photogrammetry. *Earth Surface Processes and Landforms*, 42(2), 355–364. <https://doi.org/10.1002/esp.4060>
- Dudley, P. N., John, S. N., Daniels, M. E., & Danner, E. M. (2022). Using decades of spawning data and hydraulic models to construct a temperature-dependent resource selection function for management of an endangered salmonid. *Canadian Journal of Fisheries and Aquatic Sciences*, 79(1), 73–81. <https://doi.org/10.1139/cjfas-2021-0022>
- Fausch, K. D., Torgersen, C. E., Baxter, C. V., & Li, H. W. (2002). Landscapes to riverscapes: Bridging the gap between research and conservation of stream fishes: A continuous view of the river is needed to understand how processes interacting among scales set the context for stream fishes and their habitat. *BioScience*, 52(6), 483–498. [https://doi.org/10.1641/0006-3568\(2002\)052\[0483:LTRBTG\]2.0.CO;2](https://doi.org/10.1641/0006-3568(2002)052[0483:LTRBTG]2.0.CO;2)
- García, M. H. (2008). Sediment transport and morphodynamics. In M. H. García (Ed.), *Sedimentation engineering* (pp. 21–163). ASCE. <https://doi.org/10.1061/9780784408148.ch02>
- Gard, M. (2014). Modelling changes in salmon habitat associated with river channel restoration and flow-induced channel alterations. *River Research and Applications*, 30(1), 40–44. <https://doi.org/10.1002/rra.2642>
- Geist, D. R., Brown, R. S., Cullinan, V. I., Mesa, M. G., VanderKooi, S. P., & McKinstry, C. A. (2003). Relationships between metabolic rate, muscle electromyograms and swim performance of adult Chinook salmon. *Journal of Fish Biology*, 63(4), 970–989. <https://doi.org/10.1046/j.1095-8649.2003.00217.x>
- Hafs, A. W., Harrison, L. R., Utz, R. M., & Dunne, T. (2014). Quantifying the role of woody debris in providing bioenergetically favorable habitat for juvenile salmon. *Ecological Modelling*, 285, 30–38. <https://doi.org/10.1016/j.ecolmodel.2014.04.015>
- Harrison, L. R., Bray, E., Overstreet, B., Legleiter, C. J., Brown, R. A., Merz, J. E., et al. (2019). Physical controls on salmon redd site selection in restored reaches of a regulated, gravel-bed river. *Water Resources Research*, 55(11), 8942–8966. <https://doi.org/10.1029/2018wr024428>
- Hayes, J. W., Hughes, N. F., & Kelly, L. H. (2007). Process-based modelling of invertebrate drift transport, net energy intake and reach carrying capacity for drift-feeding salmonids. *Ecological Modelling*, 207(2–4), 171–188. <https://doi.org/10.1016/j.ecolmodel.2007.04.032>

- Headwall Photonics. (2018). Nano-hyperspec. Retrieved from <http://www.headwallphotonics.com/spectral-imaging/hyperspectral/nano-hyperspec>
- ITRES. (2014). CASI-1500 hyperspectral imager. Retrieved from <http://www.itres.com/products/imagers/casi1500/>
- Javernick, L., Hicks, D. M., Measures, R., Caruso, B., & Brasington, J. (2016). Numerical modelling of braided rivers with Structure-from-Motion-derived terrain models. *River Research and Applications*, 32(5), 1071–1081. <https://doi.org/10.1002/rra.2918>
- Jowett, I. G., Hayes, J. W., & Neuswanger, J. (2021). Salmonid bioenergetic drift-foraging: Swimming costs and capture success. *Journal of Ecohydraulics*, 6(2), 186–197. <https://doi.org/10.1080/24705357.2020.1839799>
- Kammel, L. E., Pasternack, G. B., Massa, D. A., & Bratovich, P. M. (2016). Near-census ecohydraulics bioverification of *Oncorhynchus mykiss* spawning microhabitat preferences. *Journal of Ecohydraulics*, 1(1–2), 62–78. <https://doi.org/10.1080/24705357.2016.1237264>
- Kasvi, E., Alho, P., Lotsari, E., Wang, Y., Kukko, A., Hyypää, H., & Hyypää, J. (2015). Two-dimensional and three-dimensional computational models in hydrodynamic and morphodynamic reconstructions of a river bend: Sensitivity and functionality. *Hydrological Processes*, 29(6), 1604–1629. <https://doi.org/10.1002/hyp.10277>
- Kimmerer, W., Avent, S. R., Bollens, S. M., Feyrer, F., Grimaldo, L. F., Moyle, P. B., et al. (2005). Variability in length-weight relationships used to estimate biomass of estuarine fish from survey data. *Transactions of the American Fisheries Society*, 134(2), 481–495. <https://doi.org/10.1577/T04-042.1>
- Kinzel, P. J., Legleiter, C. J., & Grams, P. E. (2021). Field evaluation of a compact, polarizing topo-bathymetric lidar across a range of river conditions. *River Research and Applications*, 37(4), 531–543. <https://doi.org/10.1002/rra.3771>
- Lague, D., & Feldmann, B. (2020). *Topo-bathymetric airborne LiDAR for fluvial-geomorphology analysis*. In P. Tarolli & S. M. Mudd (Eds.), *Remote sensing of geomorphology* (Vol. 23, pp. 25–54). Elsevier. <https://doi.org/10.1016/b978-0-444-64177-9.00002-3>
- Lane, S., Bradbrook, K., Richards, K., Biron, P., & Roy, A. (1999). The application of computational fluid dynamics to natural river channels: Three-dimensional versus two-dimensional approaches. *Geomorphology*, 29(1), 1–20. [https://doi.org/10.1016/S0169-555X\(99\)00003-3](https://doi.org/10.1016/S0169-555X(99)00003-3)
- Legleiter, C. J. (2021). The optical river bathymetry toolkit. *River Research and Applications*, 37(4), 555–568. <https://doi.org/10.1002/rra.3773>
- Legleiter, C. J., & Fosness, R. L. (2019). Defining the limits of spectrally based bathymetric mapping on a large river. *Remote Sensing*, 11(6), 665. <https://doi.org/10.3390/rs11060665>
- Legleiter, C. J., & Harrison, L. R. (2019a). Remote sensing of river bathymetry: Evaluating a range of sensors, platforms, and algorithms on the Upper Sacramento River, California, USA. *Water Resources Research*, 55(3), 2142–2169. <https://doi.org/10.1029/2018wr023586>
- Legleiter, C. J., & Harrison, L. R. (2019b). Remotely sensed data and field measurements used for bathymetric mapping of the Upper Sacramento River in northern California Dataset. *U.S. Geological Survey Data Release*. <https://doi.org/10.50666/F7Q52NZ1>
- Legleiter, C. J., & Harrison, L. R. (2022). Digital elevation models (DEMs) and field measurements of flow velocity used to develop and test multi-dimensional hydrodynamic models (2D and 3D) for a reach of the Upper Sacramento River in northern California Dataset. *U.S. Geological Survey Data Release*. <https://doi.org/10.50666/P946FW28>
- Legleiter, C. J., Roberts, D. A., & Lawrence, R. L. (2009). Spectrally based remote sensing of river bathymetry. *Earth Surface Processes and Landforms*, 34(8), 1039–1059. <https://doi.org/10.1002/esp.1787>
- Lennox, R. J., Eliason, E. J., Havn, T. B., Johansen, M. R., Thorstad, E. B., Cooke, S. J., et al. (2018). Bioenergetic consequences of warming rivers to adult Atlantic salmon *Salmo salar* during their spawning migration. *Freshwater Biology*, 63(11), 1381–1393. <https://doi.org/10.1111/fwb.13166>
- Lyzenga, D. R. (1978). Passive remote-sensing techniques for mapping water depth and bottom features. *Applied Optics*, 17(3), 379–383. <https://doi.org/10.1364/AO.17.000379>
- MacFarlane, R. B., & Norton, E. C. (2002). Physiological ecology of juvenile Chinook salmon (*Oncorhynchus tshawytscha*) at the southern end of their distribution, the San Francisco Estuary and Gulf of the Farallones, California. *California Fisheries Bulletin*, 100, 244–257.
- Mandlburger, G., Hauer, C., Wieser, M., & Pfeifer, N. (2015). Topo-bathymetric LiDAR for monitoring river morphodynamics and instream habitats—A case study at the Pielach River. *Remote Sensing*, 7(5), 6160–6195. <https://doi.org/10.3390/rs70506160>
- Mandlburger, G., Pfennigbauer, M., Schwarz, R., Flöry, S., & Nussbaumer, L. (2020). Concept and performance evaluation of a novel UAV-borne topo-bathymetric lidar sensor. *Remote Sensing*, 12(6), 986. <https://doi.org/10.3390/rs12060986>
- Martyr-Koller, R. C., Kernkamp, H. W. J., Van Dam, A., Van der Wegen, M., Lucas, L. V., Knowles, N., et al. (2017). Application of an unstructured 3D finite volume numerical model to flows and salinity dynamics in the San Francisco Bay-delta. *Estuarine, Coastal and Shelf Science*, 192, 86–107. <https://doi.org/10.1016/j.ecss.2017.04.024>
- May, C. L., Pryor, B., Lisle, T. E., & Lang, M. (2009). Coupling hydrodynamic modeling and empirical measures of bed mobility to predict the risk of scour and fill of salmon redds in a large regulated river. *Water Resources Research*, 45(5). <https://doi.org/10.1029/2007WR006498>
- May, C. L., & Pryor, B. S. (2016). Explaining spatial patterns of mussel beds in a northern California River: The role of flood disturbance and spawning salmon. *River Research and Applications*, 32(4), 776–785. <https://doi.org/10.1002/rra.2894>
- McKean, J., Nagel, D., Tonina, D., Bailey, P., Wright, C. W., Bohn, C., & Nayegandhi, A. (2009). Remote sensing of channels and riparian zones with a narrow-beam aquatic-terrestrial LIDAR. *Remote Sensing*, 1(4), 1065–1096. <https://doi.org/10.3390/rs1041065>
- McKean, J., Tonina, D., Bohn, C., & Wright, C. W. (2014). Effects of bathymetric LiDAR errors on flow properties predicted with a multi-dimensional hydraulic model. *Journal of Geophysical Research: Earth Surface*, 119(3), 644–664. <https://doi.org/10.1002/2013jf002897>
- Michel, C. J., Ammann, A. J., Chapman, E. D., Sandstrom, P. T., Fish, H. E., Thomas, M. J., et al. (2013). The effects of environmental factors on the migratory movement patterns of Sacramento River yearling late-fall run Chinook salmon (*Oncorhynchus tshawytscha*). *Environmental Biology of Fishes*, 96(2–3), 257–271. <https://doi.org/10.1007/s10641-012-9990-8>
- Moyle, P., Lusardi, R., Samuel, P., & Katz, J. (2017). *State of the salmonids: Status of California's emblematic fishes 2017*. University of California, Davis and California Trout. Retrieved from <https://watershed.ucdavis.edu/library>
- Nelson, P. A., McDonald, R. R., Nelson, J. M., & Dietrich, W. E. (2015). Coevolution of bed surface patchiness and channel morphology: 1. Mechanisms of forced patch formation. *Journal of Geophysical Research: Earth Surface*, 120(9), 1687–1707. <https://doi.org/10.1002/2014JF003428>
- Niroumand-Jadidi, M., Vitti, A., & Lyzenga, D. R. (2018). Multiple optimal depth predictors analysis (MODPA) for river bathymetry: Findings from spectroradiometry, simulations, and satellite imagery. *Remote Sensing of Environment*, 218, 132–147. <https://doi.org/10.1016/j.rse.2018.09.022>
- Olivetti, S., Gil, M. A., Sridharan, V. K., Hein, A. M., & Shepard, E. (2021). Merging computational fluid dynamics and machine learning to reveal animal migration strategies. *Methods in Ecology and Evolution*, 12(7), 1186–1200. <https://doi.org/10.1111/2041-210X.13604>
- O'Sullivan, A. M., Wegscheider, B., Helminen, J., Cormier, J. G., Linnansaari, T., Wilson, D. A., & Curry, R. A. (2021). Catchment-scale, high-resolution, hydraulic models and habitat maps – A salmonid's perspective. *Journal of Ecohydraulics*, 6(1), 53–68. <https://doi.org/10.1080/24705357.2020.1768600>

- Parsons, D. R., Jackson, P. R., Czuba, J. A., Engel, F. L., Rhoads, B. L., Oberg, K. A., et al. (2013). Velocity mapping toolbox (VMT): A processing and visualization suite for moving-vessel ADCP measurements. *Earth Surface Processes and Landforms*, 38(11), 1244–1260. <https://doi.org/10.1002/esp.3367>
- Passalacqua, P., Belmont, P., Staley, D. M., Simley, J. D., Arrowsmith, J. R., Bode, C. A., et al. (2015). Analyzing high resolution topography for advancing the understanding of mass and energy transfer through landscapes: A review. *Earth-Science Reviews*, 148, 174–193. <https://doi.org/10.1016/j.earscirev.2015.05.012>
- Pasternack, G. B. (2019). Applied fluvial ecohydraulics. In E. Wohl (Ed.), *Oxford bibliographies in environmental science* (p. 42). Oxford University Press. <https://doi.org/10.1093/OBO/9780199363445-0124>
- Pasternack, G. B., & Senter, A. (2011). 21st century instream flow assessment framework for mountain streams. *California Energy Commission*, PIER. CEC-500-2013-059, 463. Retrieved from <https://lcn.loc.gov/2014486511>
- Piégay, H., Arnaud, F., Belletti, B., Bertrand, M., Bizzi, S., Carbonneau, P., et al. (2020). Remotely sensed rivers in the Anthropocene: State of the art and prospects. *Earth Surface Processes and Landforms*, 45(1), 157–188. <https://doi.org/10.1002/esp.4787>
- Poytress, W. R. (2016). *Brood-year 2014 winter Chinook juvenile production indices with comparisons to juvenile production estimates derived from adult escapement*. U.S. Fish and Wildlife Service. <https://doi.org/10.1017/CBO9781107415324.004>
- Reeder, W. J., Gariglio, F., Carnie, R., Tang, C., Isaak, D., Chen, Q., et al. (2021). Some (fish might) like it hot: Habitat quality and fish growth from past to future climates. *Science of the Total Environment*, 787, 147532. <https://doi.org/10.1016/j.scitotenv.2021.147532>
- Rombough, P. J., & Ure, D. (1991). Partitioning of oxygen uptake between cutaneous and branchial surfaces in larval and young juvenile Chinook salmon *Oncorhynchus tshawytscha*. *Physiological Zoology*, 64(3), 717–727. <https://doi.org/10.1086/physzool.64.3.30158203>
- Schuurman, F., Ta, W., Post, S., Sokolewicz, M., Busnelli, M., & Kleinhans, M. (2018). Response of braiding channel morphodynamics to peak discharge changes in the Upper Yellow River. *Earth Surface Processes and Landforms*, 43(8), 1648–1662. <https://doi.org/10.1002/esp.4344>
- Shimizu, Y., Nelson, J., Arnez Ferrel, K., Asahi, K., Giri, S., Inoue, T., et al. (2020). Advances in computational morphodynamics using the international river interface cooperative (iRIC) software. *Earth Surface Processes and Landforms*, 45(1), 11–37. <https://doi.org/10.1002/esp.4653>
- Singer, M. B. (2008). Downstream patterns of bed material grain size in a large, lowland alluvial river subject to low sediment supply. *Water Resources Research*, 44, W12202. <https://doi.org/10.1029/2008WR007183>
- Tamminga, A., Hugenholtz, C., Eaton, B., & Lapointe, M. (2015). Hyperspatial remote sensing of channel reach morphology and hydraulic fish habitat using an unmanned aerial vehicle (UAV): A first assessment in the context of river research and management. *River Research and Applications*, 31(3), 379–391. <https://doi.org/10.1002/rra.2743>
- Thorarensen, H., & Farrell, A. (2006). Postprandial intestinal blood flow, metabolic rates, and exercise in Chinook salmon (*Oncorhynchus tshawytscha*). *Physiological and Biochemical Zoology*, 79(4), 688–694. <https://doi.org/10.1086/505512>
- Tonina, D., & Jorde, K. (2013). Hydraulic modelling approaches for ecohydraulic studies: 3D, 2D, 1D and non-numerical models. In I. Maddock, A. Harby, P. Kemp, & P. Wood (Eds.), *Ecohydraulics* (pp. 31–74). John Wiley & Sons, Ltd. <https://doi.org/10.1002/9781118526576.ch3>
- Tonina, D., McKean, J. A., Benjankar, R. M., Wright, C. W., Goode, J. R., Chen, Q., et al. (2018). Mapping river bathymetries: Evaluating topobathymetric LiDAR survey. *Earth Surface Processes and Landforms*, 44(2), 507–520. <https://doi.org/10.1002/esp.4513>
- Tonina, D., McKean, J. A., Benjankar, R. M., Yager, E., Carmichael, R. A., Chen, Q., et al. (2020). Evaluating the performance of topobathymetric LiDAR to support multi-dimensional flow modelling in a gravel-bed mountain stream. *Earth Surface Processes and Landforms*, 45(12), 2850–2868. <https://doi.org/10.1002/esp.4934>
- Torgersen, C. E., Le Pichon, C., Fullerton, A. H., Dugdale, S. J., Duda, J. J., Giovannini, F., et al. (2022). Riverscape approaches in practice: Perspectives and applications. *Biological Reviews*, 97(2), 481–504. <https://doi.org/10.1111/brv.12810>
- USFWS. (2005). *Flow-habitat relationships for Chinook salmon rearing in the Sacramento River between Keswick Dam and Battle Creek*. U.S. Fish and Wildlife Service.
- U.S. Geological Survey. (2022). *USGS water data for the nation: U.S. Geological survey National water information system database*. U.S. Geological Survey. <https://doi.org/10.5066/F7P55KJN>
- Vargas-Luna, A., Crosato, A., Anders, N., Hoitink, A. J., Keesstra, S. D., & Uijtewaal, W. S. (2018). Morphodynamic effects of riparian vegetation growth after stream restoration. *Earth Surface Processes and Landforms*, 43(8), 1591–1607. <https://doi.org/10.1002/esp.4338>
- Wegscheider, B., Linnansaari, T., Ndong, M., Haralampides, K., St-Hilaire, A., Schneider, M., & Curry, R. A. (2021). Fish habitat modelling in large rivers: Combining expert opinion and hydrodynamic modelling to inform river management. *Journal of Ecohydraulics*, 0(0), 1–19. <https://doi.org/10.1080/24705357.2021.1938251>
- Wheaton, J. M., Bouwes, N., McHugh, P., Saunders, C., Bangen, S., Bailey, P., et al. (2018). Upscaling site-scale ecohydraulic models to inform salmonid population-level life cycle modeling and restoration actions - Lessons from the Columbia River Basin. *Earth Surface Processes and Landforms*, 43(1), 21–44. <https://doi.org/10.1002/esp.4137>
- Willemsen, P. W. J. M., Smits, B. P., Borsje, B. W., Herman, P. M. J., Dijkstra, J. T., Bouma, T. J., & Hulscher, S. J. M. H. (2022). Modeling decadal salt marsh development: Variability of the salt marsh edge under influence of waves and sediment availability. *Water Resources Research*, 58(1), e2020WR028962. <https://doi.org/10.1029/2020WR028962>
- Williams, R. D., Brasington, J., Hicks, M., Measures, R., Rennie, C. D., & Vericat, D. (2013). Hydraulic validation of two-dimensional simulations of braided river flow with spatially continuous aDcp data. *Water Resources Research*, 49(9), 5183–5205. <https://doi.org/10.1002/wrcr.20391>
- Williams, R. D., Measures, R., Hicks, D. M., & Brasington, J. (2016). Assessment of a numerical model to reproduce event-scale erosion and deposition distributions in a braided river. *Water Resources Research*, 52(8), 6621–6642. <https://doi.org/10.1002/2015WR018491>
- Winterbottom, S. J., & Gilvear, D. J. (1997). Quantification of channel bed morphology in gravel-bed rivers using airborne multispectral imagery and aerial photography. *Regulated Rivers: Research & Management*, 13(6), 489–499. [https://doi.org/10.1002/\(SICI\)1099-1646\(199711/12\)13:6<489::AID-RRR471>3.0.CO;2-X](https://doi.org/10.1002/(SICI)1099-1646(199711/12)13:6<489::AID-RRR471>3.0.CO;2-X)
- Woodget, A. S., Carbonneau, P. E., Visser, F., & Maddock, I. P. (2015). Quantifying submerged fluvial topography using hyperspatial resolution UAS imagery and structure from motion photogrammetry. *Earth Surface Processes and Landforms*, 40(1), 47–64. <https://doi.org/10.1002/esp.3613>
- Woodget, A. S., Fyffe, C., & Carbonneau, P. E. (2018). From manned to unmanned aircraft: Adapting airborne particle size mapping methodologies to the characteristics of sUAS and SfM. *Earth Surface Processes and Landforms*, 43(4), 857–870. <https://doi.org/10.1002/esp.4285>
- Yoshiyama, R. M., Fisher, F. W., & Moyle, P. B. (1998). Historical abundance and decline of Chinook salmon in the Central Valley region of California. *North American Journal of Fisheries Management*, 18(3), 487–521. [https://doi.org/10.1577/1548-8675\(1998\)018<0487:haadoc>2.0.co;2;2](https://doi.org/10.1577/1548-8675(1998)018<0487:haadoc>2.0.co;2;2)
- Yurok Tribe. (2018). *Topographic data set: Klamath River, California*. Distributed by OpenTopography. <https://doi.org/10.5069/G9DN436N>